

General Disclaimer

One or more of the Following Statements may affect this Document

- This document has been reproduced from the best copy furnished by the organizational source. It is being released in the interest of making available as much information as possible.
- This document may contain data, which exceeds the sheet parameters. It was furnished in this condition by the organizational source and is the best copy available.
- This document may contain tone-on-tone or color graphs, charts and/or pictures, which have been reproduced in black and white.
- This document is paginated as submitted by the original source.
- Portions of this document are not fully legible due to the historical nature of some of the material. However, it is the best reproduction available from the original submission.

A CALIBRATION AND DIAGNOSIS OF THE TEST STREAM
OF AN ELECTRIC ARC-HEATED WIND TUNNEL

A Thesis

Presented to

the Faculty of the School of Engineering and Applied Science
University of Virginia

In Partial Fulfillment
of the Requirements for the Degree
Master of Aerospace Engineering

by

Robert W. Guy

September 1969



FACILITY FORM 602	N70-25367	(THRU)
	(ACCESSION NUMBER)	1
	113 (PAGES)	(CODE)
	TMX #62841 (NASA CR OR TMX OR AD NUMBER)	12 (CATEGORY)

APPROVAL SHEET

This thesis is submitted in partial fulfillment of
the requirements for the degree of
Master of Aerospace Engineering

Author

APPROVED:

Faculty Advisor

Dean, School of Engineering and
Applied Science

September 1969

ABSTRACT

An experimental investigation has been performed to establish the state of the gas in the nozzle expansion of air in a hypersonic arc-heated wind tunnel. Tests covered ranges of stagnation chamber pressure from 4.20 to 9.38 atmospheres and stagnation enthalpies from 700 to 3,510 Btu/lbm. Parameters measured during the tests were N_2 vibrational temperature, N_2 rotational temperature, static pressure, static density, velocity, total enthalpy, and hemisphere stagnation-point heating rate. Results of the tests indicate general agreement with a chemical nonequilibrium, vibrational sudden-freeze model for the expansion of the air in the nozzle.

ACKNOWLEDGMENTS

The author is indebted to the National Aeronautics and Space Administration for permission to use material obtained from a research project at Langley Research Center in this thesis.

The author would like to gratefully acknowledge that Mr. Daniel I. Sebacher of this laboratory operated the electron beam-spectrometer apparatus and contributed his expertise in electron-beam technology in obtaining some of the data.

The conscientious efforts of Louise P. Lee in programing and processing some of the computer programs used in this thesis are acknowledged with much appreciation.

The author is also indebted to Dr. J. O. Bunting of the University of Virginia for his comments and helpful assistance in the preparation of this thesis.

Finally, the author wishes to express his gratitude to his wife, Diane, for her patient support, encouragement, and many late hours spent in typing the original manuscript.

TABLE OF CONTENTS

CHAPTER	PAGE
I. INTRODUCTION	1
II. APPARATUS AND TESTS	4
Tunnel	4
Test Conditions	7
Models and Instrumentation	8
Total calorimeter	8
Electron-beam apparatus	9
Wall static pressure measurements	10
Mass flow probe	12
Stagnation point heat-transfer probe	15
Test Procedure	17
III. DATA REDUCTION	19
Calorimeter	19
Vibrational Temperature	20
Rotational Temperature	24
Wall Static Pressure	29
Pitot Pressure	34
Density and Velocity	34
Stagnation Point Heat Transfer	37

CHAPTER	PAGE
IV. THEORY	41
Enthalpy Determination	41
Plenum chamber	41
Test section	42
Gas Flow Models	47
Equilibrium flow	49
Nonequilibrium flow	49
Frozen flow	57
V. RESULTS AND DISCUSSION	58
Calorimeter Data	58
Stagnation Point Heat Transfer	62
Vibrational Temperature	65
Rotational Temperature	68
Nozzle Wall Static Pressures	72
Static Density	76
Velocity	79
Pitot Pressure Gradients	79
VI. CONCLUDING REMARKS	84
REFERENCES	87
APPENDIX - EXPERIMENTAL DATA FOR ALL TESTS	92

LIST OF FIGURES

FIGURE		PAGE
1.	Schematic drawing of the Langley 1-foot hypersonic arc tunnel	5
2.	Schematic drawing of the electron beam-spectrometer apparatus attached to the tunnel	11
3.	Schematic drawing of the shock-swallowing mass flow probe	13
4.	Schematic drawing of the stagnation point heat-transfer rate probe	16
5.	Curves for the determination of total enthalpy by the equilibrium sonic-throat method	21
6.	Ratio of the relative intensities of the (0,1) and (1,2) vibrational bands of electron-beam excited N_2^+ as a function of vibrational temperature of N_2	22
7.	A typical spectrometer record of the relative intensities of the (0,1) and (1,2) vibrational bands of electron-beam excited N_2^+	23
8.	A typical spectrometer record of the rotational lines of the (0,0) vibrational band of electron-beam excited N_2^+	25
9.	Variation of $\log_e(I/K'v^4G)$ with $K'(K' + 1)$ for the (0,0) vibrational band of N_2^+ to determine the free-stream rotational temperature of N_2	30

FIGURE

PAGE

10. Examples of boundary-layer contouring for an equilibrium expansion in a 5° half-angle conical nozzle
($d^* = 0.212$ inch) 32
11. Pitot pressure surveys across the test section for a range of test conditions (surveys taken 2-1/4 inches from nozzle exit) 33
12. Photographs of the mass flow probe tip illustrating the disappearance of the stagnation region gas cap when applying a very low downstream pressure to the probe . . 35
13. Actual shape of the tip of the stagnation point heat-transfer probe and the shapes used to define the limits of the effective hemisphere 38
14. Variation of species mass fraction with nozzle area ratio. ($P_{t,1} = 9.78$ atm, $T_{t,1} = 7810^\circ$ R) 52
 - (a) Dominant species ($C_{AR} = 0.0128598 = \text{constant}$). 52
 - (b) Species with smaller mass fractions 53
15. A comparison of total enthalpy as calculated by the equilibrium sonic-throat method with that determined from a total calorimeter 60
16. Variation of the difference between arc chamber centerline and outside wall pressure with total enthalpy 61
17. A comparison of measured stagnation point heat-transfer rate with theory 63

FIGURE

PAGE

18.	Measurements of N_2 vibrational temperature illustrating the nonequilibrium nozzle flow	66
	(a) Dimensional data	66
	(b) Dimensionless data	67
19.	A comparison of measured N_2 rotational temperature with theoretical predictions of the nozzle expansions of gas models ranging from frozen to equilibrium	69
	(a) Dimensional data	69
	(b) Dimensionless data	70
20.	A comparison of measured wall static pressure with theoretical predictions of the nozzle expansions of gas models ranging from frozen to equilibrium	73
	(a) Dimensional data	73
	(b) Dimensionless data	74
21.	A comparison of measured static density with theoretical predictions of the nozzle expansions of gas models ranging from frozen to equilibrium	77
	(a) Dimensional data	77
	(b) Dimensionless data	78
22.	A comparison of measured free-stream velocity with theoretical predictions of the nozzle expansions of gas models ranging from frozen to equilibrium	80
	(a) Dimensional data	80
	(b) Dimensionless data	81

FIGURE

PAGE

23. Axial pitot pressure distribution as a function of

total enthalpy 82

LIST OF TABLES

TABLE	PAGE
I. Chemical Reactions Used in the Nonequilibrium Nozzle	
Flow Program	51
II. Experimental Results From the Total Calorimeter Tests . .	93
III. Experimental Results From the Stagnation Point Heat-	
Transfer Rate Tests	94
IV. Experimental Results From the N ₂ Vibrational Temperature	
Tests	95
V. Experimental Results From the N ₂ Rotational Temperature	
Tests	96
VI. Experimental Results From the Wall Static Pressure	
Tests	97
VII. Experimental Results From the Mass Flow Probe Tests . . .	98

LIST OF SYMBOLS

A	cross-sectional area; also, constant in Equation (20)
A_1	constant in Equation (27)
A_2	constant in Equation (27)
B	constant in Equation (4)
C	mass fraction
C_1	defined by Equation (23)
C_1^*	Damköhler ratio for boundary-layer recombination
C_p	specific heat at constant pressure
C_v	specific heat at constant volume
d	orifice diameter
D	probe outer diameter
Da_d	Damköhler ratio for dissociation in the shock layer
Da_v	Damköhler ratio for vibrational excitation in the shock layer
E	vibrational energy
G	function of K' and T_R (specified in Refs.)
H	total enthalpy
h	static enthalpy
$I_{K',K''}$	intensity of radiation of rotational transitions between $N_2^+B^2\Sigma$ and $N_2^+X^2\Sigma$
$I_{Z,F1}, I_{Z,F2}, I_{Z,F3}$	reaction rate integrals for frozen flow (Ref. 49)
$j = 0$	for two-dimensional flow
$j = 1$	for axisymmetric flow

K_R	recombination rate constant
K_w	surface catalytic reaction rate constant
K'	rotational quantum number for the $N_2^+B^2\Sigma$ state
K''	rotational quantum number for the $N_2^+X^2\Sigma$ state
Le	Lewis number
L_w	Damköhler number for surface reaction
M	Mach number
MW	molecular weight
\dot{m}	mass flow rate
P	pressure
Pr	Prandtl number
\dot{q}	heat-transfer rate
R_s	specific gas constant
R_B	body radius
R_C	corner radius
R_H	radius of a hemisphere
R_N	nose radius
R_A	partial specific gas constant defined by Equation (30)
R_M	partial specific gas constant defined by Equation (29)
R_u	universal gas constant
Re	Reynolds number
S	diffusion velocity in boundary layer
Sc	Schmidt number
T	temperature
T_D	characteristic dissociation temperature

T_0	standard temperature, 491.69° R
T_R	rotational temperature
T_V	vibrational temperature
t	time
V	velocity
V_∞	limiting velocity, $\sqrt{2H_{t,1}}$
x	longitudinal coordinate
y	lateral coordinate
Z	compressibility factor
α	dissociation mass fraction
β	inviscid velocity gradient at the stagnation point
γ	ratio of specific heats
δ^*	boundary-layer displacement thickness
$\Delta h_{\text{chem,max}}$	enthalpy in dissociation at the boundary layer edge
ΔT	temperature difference
η	concentration in units of moles of species per mass of mixture
θ_{ROT}	characteristic rotational temperature
μ	viscosity
ρ	density
ϕ	extent of recombination
τ_V	vibrational relaxation time
$\nu_{K',K''}$	wave number
ω	exponent defining the temperature dependence of K_r

Subscripts:

a	air
B.L.	boundary layer
c	cold flow conditions (arc off)
CAL	pertaining to the total calorimeter
CL	centerline
CT	contamination trap
e	edge of boundary layer
eff	effective
f	chemistry and vibration frozen behind normal shock
h	hot flow conditions (arc on)
p	probe
sonic throat	pertaining to the equilibrium sonic-throat technique
t	stagnation conditions
t,1	stagnation conditions in the undisturbed, isentropic free stream
t,2	stagnation conditions behind a normal shock
w	conditions at the wall; or water
∞	free-stream conditions
2	conditions just behind a normal shock
Ar	argon
E ⁻	electron
N	atomic nitrogen
N ₂	molecular nitrogen

NO nitric oxide

NO⁺ nitric oxide ion

O atomic oxygen

O₂ molecular oxygen

Superscripts:

* tunnel throat conditions ($M_{\infty} = 1$)

' pertaining to conditions at the vibrational
 freezing-point station

CHAPTER I

INTRODUCTION

The age of high-speed ballistic missiles and space travel has caused considerable interest in the phenomena occurring during hypervelocity flight in planetary atmospheres, especially the earth's atmosphere. The design of these vehicles requires a knowledge of the surrounding flow field.

Although flight tests have been made to investigate the problems, ground facilities are used most extensively to acquire the needed data. Therefore, much effort has gone into developing wind tunnels that will simulate portions of the flight paths of various hypervelocity vehicles. Shock tubes, hotshot tunnels, expansion tubes, and arc-heated wind tunnels are among the devices that are used to study high-speed phenomena.

A major problem encountered in simulating these high-speed flight conditions in wind tunnels is that thermal energy must be converted to kinetic energy by expanding the heated gas in a nozzle. Prior to entering the nozzle, the near-stagnant gas will be at a high temperature with various energy modes excited. For example, in the case of air, the total energy of the diatomic molecules will be distributed between the translational, rotational, and vibrational degrees of freedom, with energy also being absorbed in electronic excitation, dissociation, and ionization. As the gas expands down the nozzle, the expansion is

generally so rapid that the flow kinetics cannot keep pace with the rapidly changing thermodynamic state of the flow. Consequently, the gas dynamics of the flow is affected.

Generally, translation and rotation will be represented by the same kinetic temperature due to the small number of collisions required to equilibrate these modes. However, vibrational and chemical changes require many more collisions to achieve equilibrium; therefore, chemical composition and vibrational temperature will generally not correspond to the equilibrium values that would be associated with the static temperature and pressure. In turn, the values of the flow variables (pressure, temperature, density, velocity, etc.) are affected by the extent of nonequilibrium.

These nonequilibrium phenomena present the researcher in the ground facility with two problems. First, the composition of the air in the free stream of the tunnel is generally quite different from the atmospheric free stream of a flight path. Secondly, the energy that is frozen in vibration and chemistry is not available for conversion to kinetic energy.

Every effort must be made to determine the type of flow in the high-speed wind tunnels, and then the problem of nonequilibrium flow through shocks and over vehicles must be solved. These problems are rapidly becoming more severe as higher reentry velocities from distant planets must be considered.

The present work is concerned with defining the type of flow in an arc-heated wind tunnel; that is, various experimentally determined

flow properties will be compared with theoretical predictions from various gas flow models. Several authors have concerned themselves with this problem (Refs. 1 through 7). Theoretical methods for nonequilibrium flow in nozzles range from simple, sudden-freeze models to highly sophisticated models with coupling between chemistry and vibration and chemistry and electronic excitation (Refs. 8 through 14).

One can establish a priority of measurements that would contribute to an understanding of the flow. They are, in decreasing order of relative importance and sensitivity, chemical composition, static temperature and vibrational temperature, static pressure, static density, and velocity. Presently, the determination of chemical composition is ruled out since reliable spectroscopic techniques are not yet available for a flowing system (Ref. 7). N_2 rotational and vibrational temperatures can be measured using the electron beam (at low densities). Static pressures can be measured on the tunnel wall or on suitably designed probes. However, static pressure measurements can be highly uncertain in low-density flows. Density and velocity can be measured but are less sensitive to nonequilibrium effects.

The measurements taken in the present study are N_2 rotational and vibrational temperature, wall static pressures, static density, velocity, total enthalpy, and stagnation-point heating rate. The heating rates were taken in an attempt to lend credence to the values of total enthalpy used in the tests.

CHAPTER II

APPARATUS AND TESTS

Tunnel

The tunnel under investigation is the 1-Foot Hypersonic Arc Tunnel (Ref. 15) located at NASA's Langley Research Center. Flow passes from the direct-current arc heater through a circular-arc throat into a 5° half-angle conical nozzle. At the 1-foot-diameter station of the nozzle, a cylindrical test section equipped with two quartz windows (4 inches by 9-1/2 inches) is available for testing. The test section is followed by a 1-foot-diameter straight-pipe diffuser. A five-stage steam ejector provides the low back pressure for the expansion and exhausts the test gas to the atmosphere. The tunnel is a continuous-flow facility with test time limited primarily by electrode life. The tunnel is shown schematically in Figure 1.

Power for the tunnel is supplied by a 900-kilowatt direct-current generator. An additional 900 kilowatts of power is available but was not used during the present tests.

Some details of the tunnel components from the heater to the throat are presented to familiarize the reader with the specific components used, since there has been a progression of modifications to components after the publication of Reference 15.

The cathode of the heater is a 1-3/4-inch-diameter doughnut-shaped inner electrode. This electrode is cast from a 20 per cent Cu to 80 per cent Ag alloy. Test gas is injected along the sting of this

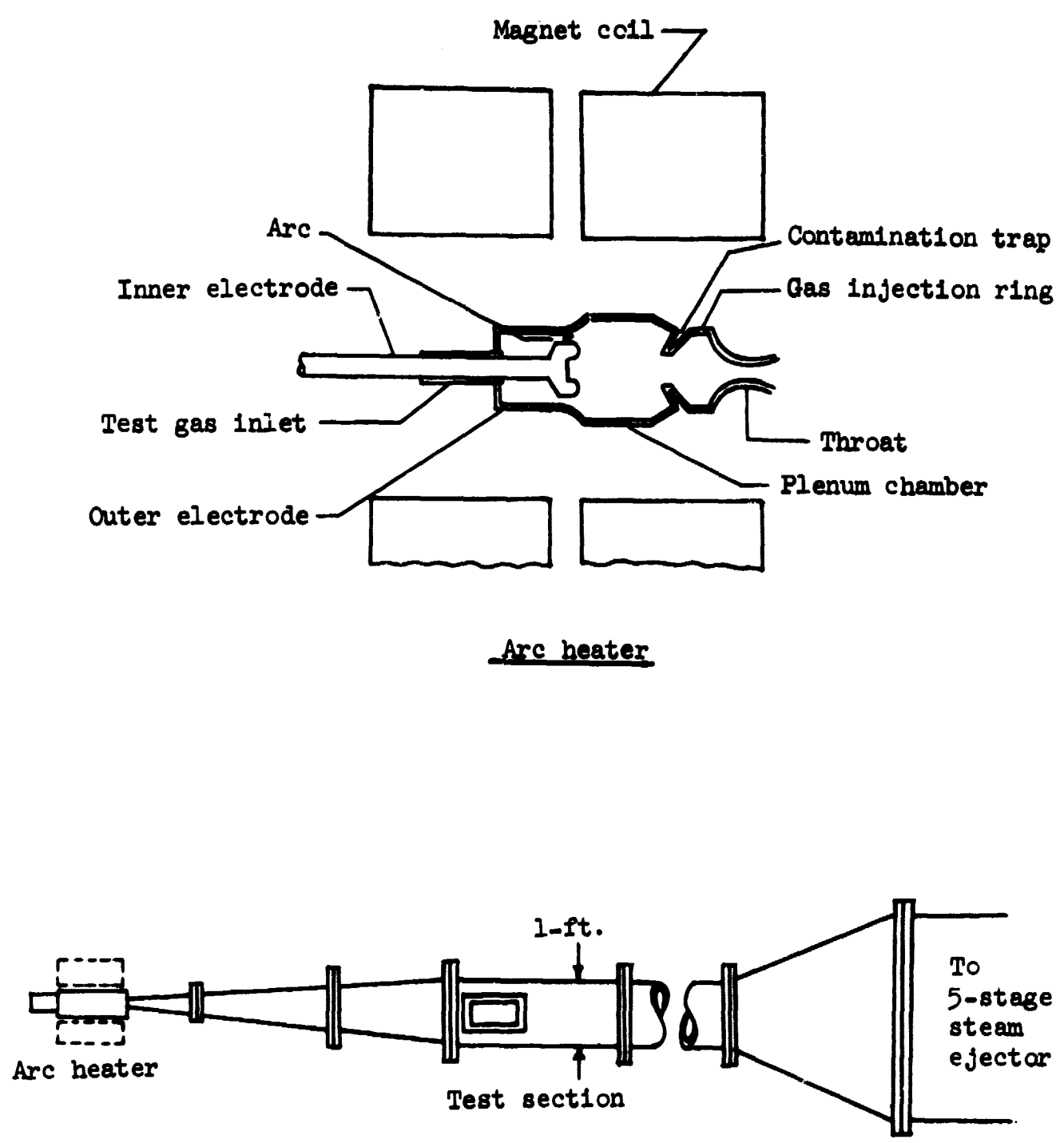


Figure 1.- Schematic drawing of the Langley 1-foot hypersonic arc tunnel.

electrode and through the arc. An orifice in the center of this electrode may be used either to measure pressure or to inject test gas.

The outer electrode (anode) used with the tunnel depends on the enthalpy level desired. Two outer electrodes, D and E, are normally used. The E electrode has an internal diameter of 2.75 inches, while the D electrode has an internal diameter of 2.38 inches. Thus, E provides a larger arc gap with increased arc voltage and higher enthalpy. Both D and E electrodes have copper internal liners. The length of E electrode is 3-1/2 inches and the length of D electrode is 3 inches.

The plenum chamber that is used with E has a stainless steel liner with an inner diameter of 3.19 inches. The plenum chamber on D electrode is an integral part of the electrode with an internal diameter of 3.25 inches. The plenum chamber length of D is 3 inches and that of E is 2-1/2 inches.

Contamination traps are used with both outer electrodes to catch some (approximately 30 per cent) of the material eroded from the inner and outer electrodes (Ref. 16). The trap that is used with D has a 1-inch aperture, while the one used with E has a 1-3/4-inch aperture. The stagnation chamber pressure is measured with an orifice located on the downstream side of the trap.

A gas injection ring is located just downstream of the contamination trap. Radially drilled holes equally spaced circumferentially inject the gas straight toward the center of the flow. This gas injection ring is used to mix cooler gas with the hot gas that has passed through the arc. This procedure allows one to obtain a further

variation of enthalpy in addition to the levels produced by the two different electrodes. The inner diameter of this ring is 2-1/2 inches and the length is 1-1/8 inches.

The gas injection ring is followed by the circular-arc throat section. Throat diameters of 0.0624, 0.125, 0.142, and 0.2115 inch are available. The 0.2115-inch-diameter throat was used for the present tests.

Two magnetic coils provide a 12,000-gauss axial magnetic field to spin the radial arc. The swirling of the arc insures electrode survival and stabilizes the arc.

All tunnel components down to and including the throat section are water cooled. Inlet and outlet cooling water temperature and the water flow rate are measured on each component.

Test Conditions

Test conditions for the present experiments will be given in terms of input parameters to the tunnel and the resulting output tunnel test conditions.

The total air mass flow through the tunnel was held constant at 0.024 lbm/sec. From 0 to 50 per cent of this flow was room-temperature dry air added through the injection ring when a variation in enthalpy was desired. The arc current was held at 1,500 amperes when outer electrode D was used. Electrode E was operated with 1,200 amperes arc current.

With these inputs, stagnation chamber pressure varied from 4.20 to 9.38 atmospheres and stagnation enthalpy varied from 700 to 3,510 Btu/lbm, thus giving a stagnation chamber temperature range from 2,665° to 8,225° R. The test section parameters of Mach number, Reynolds number, etc., are the objects of the tests and will be discussed later in the text. However, pitot pressure at a location 2-1/4 inches downstream of the nozzle-test section juncture varied from 6.3×10^{-3} to 1.2×10^{-2} atmospheres.

Models and Instrumentation

The models and measuring devices used during the present tests are listed below.

- (1) A total calorimeter for the determination of tunnel total enthalpy.
- (2) The electron-beam apparatus for the measurement of N_2 rotational and vibrational temperatures.
- (3) Static pressure orifices in the nozzle wall.
- (4) A mass flow probe for the measurement of free-stream density and velocity.
- (5) A 1-inch nose-radius-hemispherical stagnation point heat-transfer probe with a 1-inch-diameter cylindrical afterbody.
- (6) Various pitot probes in conjunction with (2), (3), (4), and (5) above.

Total calorimeter.- A total calorimeter was used to measure total enthalpy because delays in the delivery of a free-stream total

enthalpy probe prevented its use in time for inclusion in this paper and because an energy balance on the arc heater was too inaccurate a method for this facility, since the heater efficiency was less than 25 per cent. The calorimeter was attached to the downstream end of the tunnel throat section and the first two nozzle sections of the tunnel downstream of the throat were removed during the calorimeter tests.

The calorimeter was constructed of coiled copper tubing sealed with soft solder. The calorimeter inner diameter decreased from an 8-inch-long, 3-inch-inside-diameter entrance section to a constant 1-1/2-inch-inside-diameter section 12 inches long. An insert apparatus was used to decrease the flow velocity and to make more surface area available for heat transfer from the gas. Gas residual temperature was measured at the exit of the calorimeter with stainless-steel-sheathed chromel-alumel and iron-constantan thermocouples placed at various radial positions. The signal from these thermocouples was recorded on a 52-channel dry-develop oscillograph.

The inlet and outlet temperatures of the calorimeter cooling water were measured with iron-constantan thermocouples, and these temperatures were read visually by balancing a potentiometer. Calorimeter cooling water flow rate was measured with a turbine-type flow meter and the output was recorded on a recording potentiometer.

Electron beam apparatus. - A 15-kilovolt electron-beam gun and a 1/2-meter scanning spectrometer were used to measure rotational and vibrational temperature of N_2 in the test section 13 inches from the

nozzle exit. A 1-inch-diameter hemisphere-cylinder pitot probe was located 1/4 inch downstream from the beam during this series of tests.

The chamber of the gun was maintained at a pressure of approximately 10^{-6} torr by a liquid nitrogen-trapped diffusion pump. The beam width was approximately 0.060 inch and was passed in the top of the tunnel and across the stream (Fig. 2). The tunnel acted as the electron catcher. The beam current was maintained constant at 200 microamps. References 17 and 18 describe the electron-beam gun used in these tests.

A 1/2-meter scanning spectrometer was used to view the beam. Entrance and exit slit widths were adjusted to resolve the rotational lines of the (0,0) N_2^+ vibrational band in making the rotational temperature measurements. These slits were opened to get a gain in intensity so that the (0,1) N_2^+ and (1,2) N_2^+ vibrational bands were resolved in making the vibrational temperature measurements. A grating with 2,400 lines/mm (resolution of 0.2 \AA) was used on the rotational temperature studies and a grating with 600 lines/mm (resolution of 0.8 \AA) was used for the vibrational temperature studies.

Wall static pressure measurements.- The two static pressure orifices were located 6 and 6-1/2 inches upstream of the nozzle-test section juncture, respectively. One orifice was located directly above the tip of the pitot probe and the other was located 5° upstream of this point to check source flow effects. Location of the orifice upstream of the nozzle-test section juncture was required to minimize the effects of any disturbance from this juncture. The pitot probe used for the static pressure tests was a 1/4-inch-diameter flat-faced

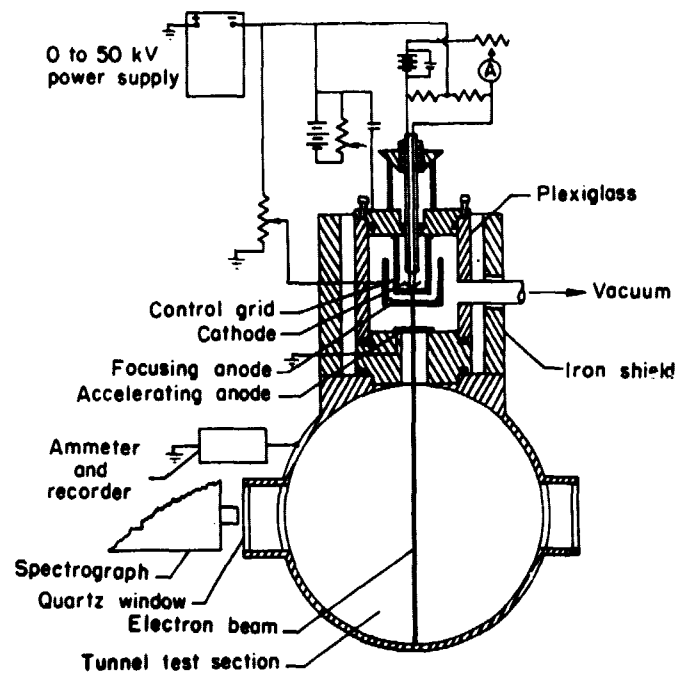


Figure 2.- Schematic drawing of the electron-beam spectrometer apparatus attached to the tunnel.

cylindrical probe 12 inches long. The probe was sufficiently small to avoid any effects of probe size on the static pressure measurements.

Static pressures and all pitot pressures were measured with capacitance-type transducers. Sensing heads of 10, 50, and 100 torr were used. The signal conditioners for these gauges provide ranges of 1.0, 0.3, 0.1, 0.03, 0.01, 0.003, 0.001, and 0.0001 of the stated head pressure. These gauges are very accurate, calibrations indicating better than 2 per cent (of the readings) agreement with the calibration standard (McLeod gauge). Comparison of the gauges on a common manifold indicated agreement between the various gauges ranging from 5 per cent at 0.030 torr to much better than 1 per cent at higher pressures.

When not in use, these gauges were at all times maintained at approximately 10^{-6} torr. Output from the pressure gauges was recorded on the 52-channel oscillograph.

Mass flow probe. - The shock-swallowing mass flow probe is shown in Figure 3. The design of this water-cooled probe is based on the results of the studies reported in Reference 19. Equal interior and exterior tip angles of 30° were used to insure that the stream tube which was swallowed was equal in cross-sectional area to the geometric inlet area of the probe (inlet diameter = 0.240 inch). The inlet section was followed by a 1/4-inch-long constant area section with a length-to-diameter ratio of 1.22. The constant area section was followed by an expanding region to a diameter of 0.431 inch. The remainder of the probe was of this diameter. This design of the entrance section gave the best results of several tips tested in Reference 19. The tip

Inlet diameter = 0.240 in. —

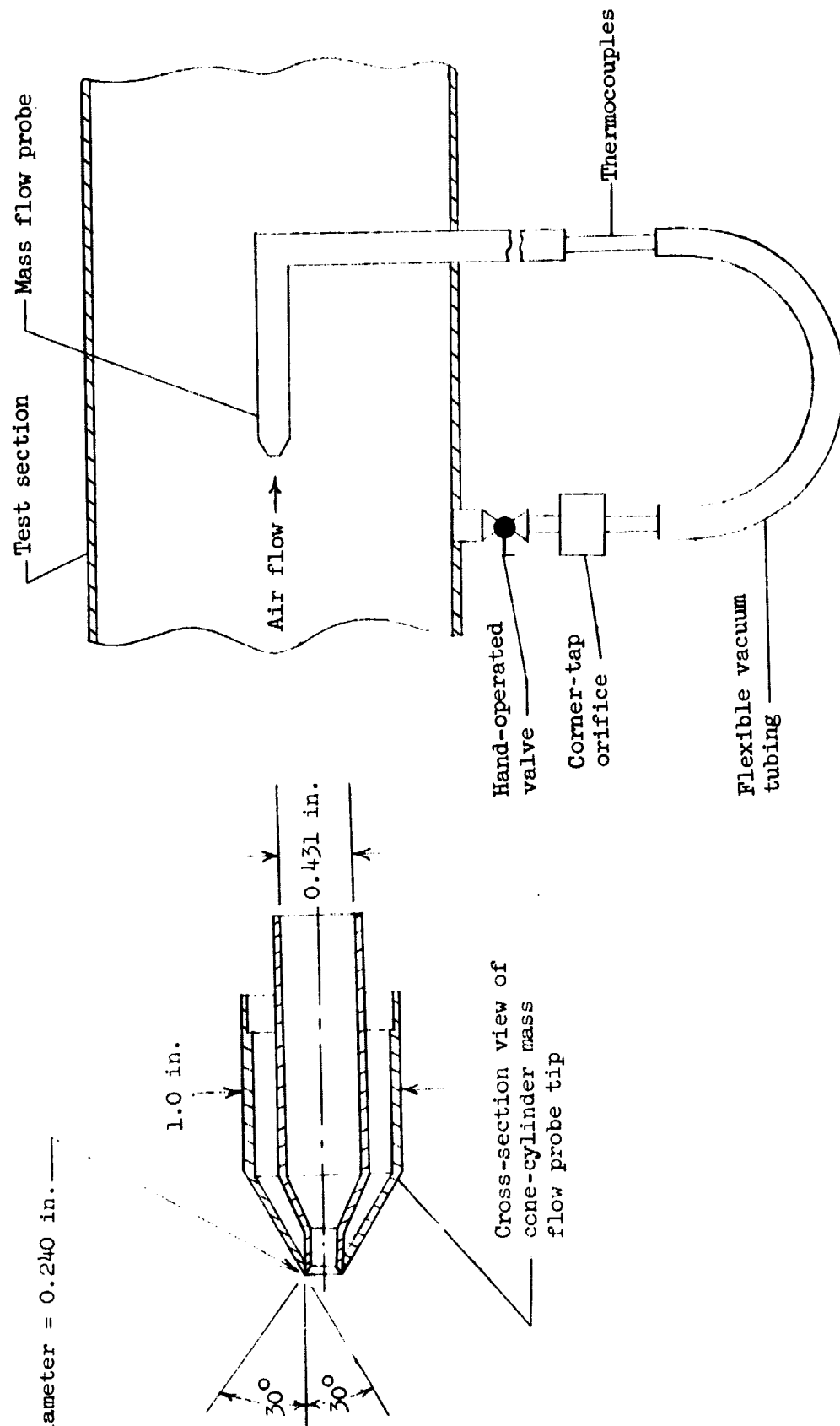


Figure 3.- Schematic drawing of the shock-swallowing mass flow probe.

design is of great importance, since viscous or bluntness effects can change the effective entrance area.

Two copper-constantan thermocouples were located near the exit of the 0.430 inner diameter tube. One thermocouple measured wall temperature, while the other measured the centerline gas temperature of the flow through the probe. The air passed the thermocouples, flowed through a piece of 1-inch I.D. flexible tygon tubing, through a flow rate measuring orifice, and back to the low static pressure of the tunnel. The tygon tubing allowed the probe to be moved so that lateral surveys could be made.

A 0.187-inch-diameter corner-tap orifice was used to measure the probe mass flow rate. The orifice was calibrated in the probe with the probe installed in the tunnel test section. Dry air was used for the calibration and a calibrated rotameter was used as the flow rate standard. Supersonic flow across the orifice was verified for the expected range of probe mass flow rates. Also, measurements of pressure drop through the probe during the orifice calibration indicated that the shock would probably be swallowed during the tests.

The capacitance pressure gauges discussed previously were used to measure pressure upstream and downstream of the orifice. These gauges were also used to measure pitot pressure when a valve downstream of the orifice meter was closed.

The 1-inch outer diameter of this water-cooled probe is compatible with the probe size used during the rotational and vibrational temperature studies. The mass flow probe was located at the same

position in the tunnel as the electron beam (13 inches from the nozzle-test section juncture).

The inlet orifice diameter of the mass flow probe was equal to the tip diameter. Thus, bleed-off effects (lowering of the pressure) when the probe was used as a pitot probe were a possible error source. Another pitot probe with the same nose shape, but with an orifice-diameter-to-tip-diameter ratio of 0.333, was built so that these pitot pressure measurements could be compared with those from the mass flow probe.

Stagnation point heat-transfer probe.- The stagnation point heat-transfer measurements were taken on a blunt cylindrical probe with $R_N/R_B = 2.0$ and $R_C/R_B = 1.0$. The probe tip was located 2-1/4 inches from the exit of the nozzle-test section juncture.

The principle of operation of the probe was that of the Gardon gauge (Ref. 20). A 0.130-inch-diameter constantan disk with a thickness of 0.015 inch was soldered to the surface of a cavity in the tip of the blunt probe (see Fig. 4). A 30-gauge copper wire was attached to the center of the disk. The cavity behind the constantan disk was a sealed insulating air pocket. Thus, cooling of the disk had to be accomplished by radial heat flow to the copper heat sink. A differential temperature exists from the center of the disk to the circle of contact with the copper when heat is applied to the tip of the probe. Thus, the heat-transfer rate is proportional to this ΔT . This heat-transfer probe was calibrated on a radiation calibration unit.

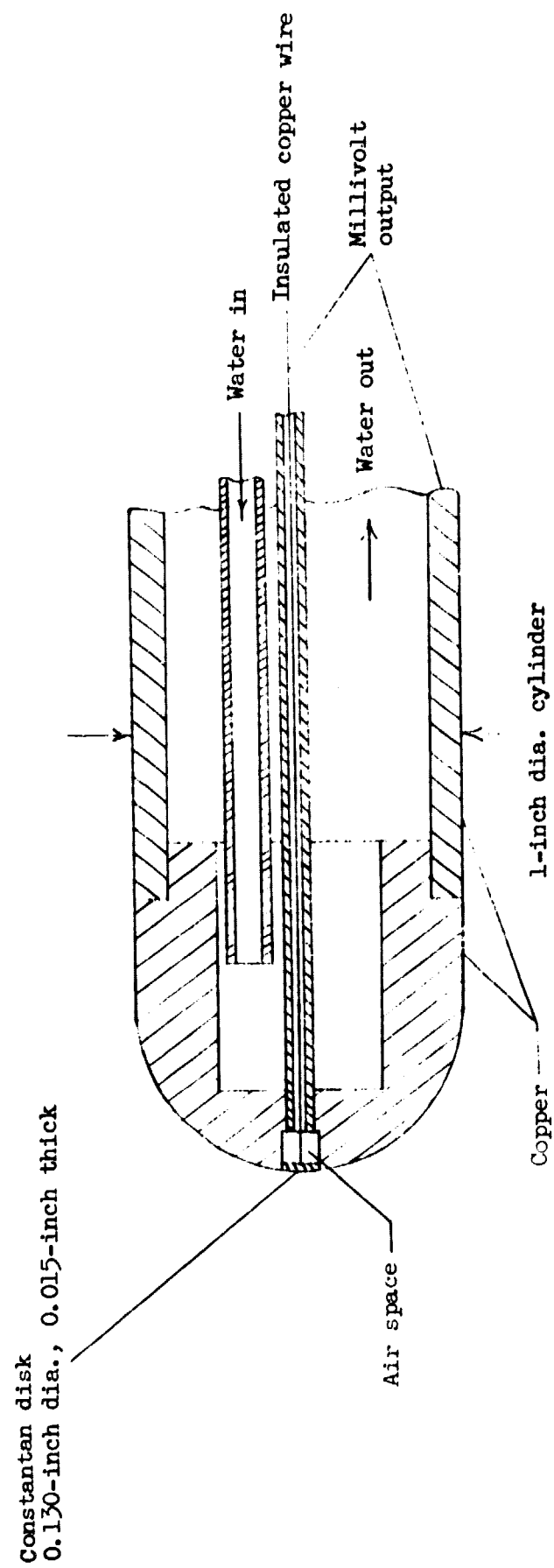


Figure 4.- Schematic drawing of the stagnation point heat-transfer rate probe.

A 1-inch-diameter pitot probe exactly like the heat-transfer probe was used on the heat-transfer tests. The probe was located at the same position in the test section as the heat-transfer probe by alternating insertion of the two probes into the stream.

Test Procedure

Prior to a test, the particular probe in use was carefully aligned with the flow on the tunnel centerline. In the case of the mass flow probe, the tip region was thoroughly cleaned before each test. Calibrate signals were applied to all associated instrumentation to insure that the equipment was functioning and that the calibrations had not changed.

The tunnel was evacuated to approximately 0.020 torr prior to a test. Cold flow was then passed through the tunnel to determine if there were any air leaks in the heater section. The arc-starter tab was also checked at this time to verify electrical contact between the inner and outer electrodes. With the cold mass flow passing through the tunnel, the arc was fired and the arc current brought up to the desired level. Tunnel-associated measurements ($P_{t,1}$, etc.) required no more than 10 seconds to stabilize. Test times ranged from approximately 30 seconds on the heat transfer and calorimeter tests to approximately 4 minutes for a rotational temperature measurement.

The calorimeter tests consisted of allowing the air-out and water-out temperatures to come to equilibrium. Then, the potentiometer measuring the water-out temperature was balanced and read visually.

The vibrational and rotational temperature measurements involved scanning the desired range of wave lengths. More than one scan was taken if any data irregularities were noticed. Pitot pressure was measured on the centerline near the end of the test.

Wall static pressures were generally measured with the 1/4-inch diameter pitot probe located on the tunnel centerline. Visual monitoring of the pressure (by use of the visual dial on the signal conditioner) was required to determine when the static pressures had stabilized.

The mass flow probe was operated with the valve open and flow passing through the probe until the upstream and downstream pressures on the flow-rate measuring orifice had stabilized. Then, the valve was closed and pitot pressure was measured.

For the stagnation point heat-transfer tests, the pitot probe was first inserted into the stream and pitot pressure was measured. This probe was then withdrawn and a measurement of heat transfer was taken by inserting the stagnation point heat-transfer probe.

After a test was completed, all capacitance pressure gauges were again switched to the vacuum pump. A cold mass flow equal to the hot mass flow was passed through the tunnel and cold stagnation chamber pressure was recorded for use in the sonic-throat enthalpy technique.

CHAPTER III

DATA REDUCTION

Calorimeter

The purpose of performing tests with the total calorimeter was to determine the total enthalpy of the flow at the entrance to the expansion (i.e., at the entrance to the convergent throat section). Any difference between the total enthalpy at this point and in the test section of the tunnel depends on the validity of the assumption of an adiabatic core of flow down the tunnel. An energy balance on the throat section, the calorimeter, and the air out of the calorimeter gives the total enthalpy at the entrance to the expansion as

$$H_{t,CAL} = H_{t,1} = \frac{(\dot{m}_w C_{p_w} \Delta T)_{throat} + (\dot{m}_w C_{p_w} \Delta T)_{CAL}}{\dot{m}_a} + C_{p_a} T_{a,out} \quad (1)$$

where the subscript *a* refers to air and the subscript *w* refers to cooling water.

The equilibrium sonic-throat technique for calculating total enthalpy was also used so that a correlation between this method and the calorimeter results could be obtained for use in later tests. Equations for total enthalpy by the sonic-throat method in equilibrium air are given in Reference 21 as functions of tunnel mass flow rate, throat area, and plenum chamber pressure. For the present tests, graphs were used to determine enthalpy at the measured pressure as a function

of $\frac{P_{t,h} \dot{m}_c}{P_{t,c} \dot{m}_h} \sqrt{T_{tc}}$ (Fig. 5). Thermodynamic data used for this plot were taken from the equilibrium throat conditions of the Cornell Aeronautical Laboratory computer program (Ref. 12). Similar plots are presented in References 21 and 22, where $H_{t,1}$ is plotted against $\frac{P_{t,1} A^*}{\dot{m}}$. A^* , in practical usage, must be the effective throat area and the use of $\frac{P_{t,h} \dot{m}_c}{P_{t,c} \dot{m}_h} \sqrt{T_{t,c}}$ in place of $\frac{P_{t,1} A^*}{\dot{m}}$ indicates that the assumption has been made that $A_{eff,c}^* = A_{eff,h}^*$ and the validity of the sonic-throat technique is dependent on this assumption.

Vibrational Temperature

The electron beam technique was used to measure free-stream nitrogen vibrational temperature in air. The vibrational temperature was determined by comparing the relative intensities of the (0,1) and (1,2) vibrational bands of N_2^+ . A plot of the relative intensity ratios, $\frac{I_{(0,1)}}{I_{(1,2)}}$, of these bands is shown in Figure 6 as a function of N_2 vibrational temperature (Ref. 17). The fact that these two bands are reasonable to use has been confirmed by Petrie (Ref. 5) and others (Refs. 17 and 23).

A typical trace obtained from the scanning spectrometer is shown in Figure 7. The ratio of the intensities of the vibrational bands was determined by ratioing the areas contained within the bands. If any irregularities occurred during the test (such as beam fluctuations), the test was prolonged and the scan was repeated.

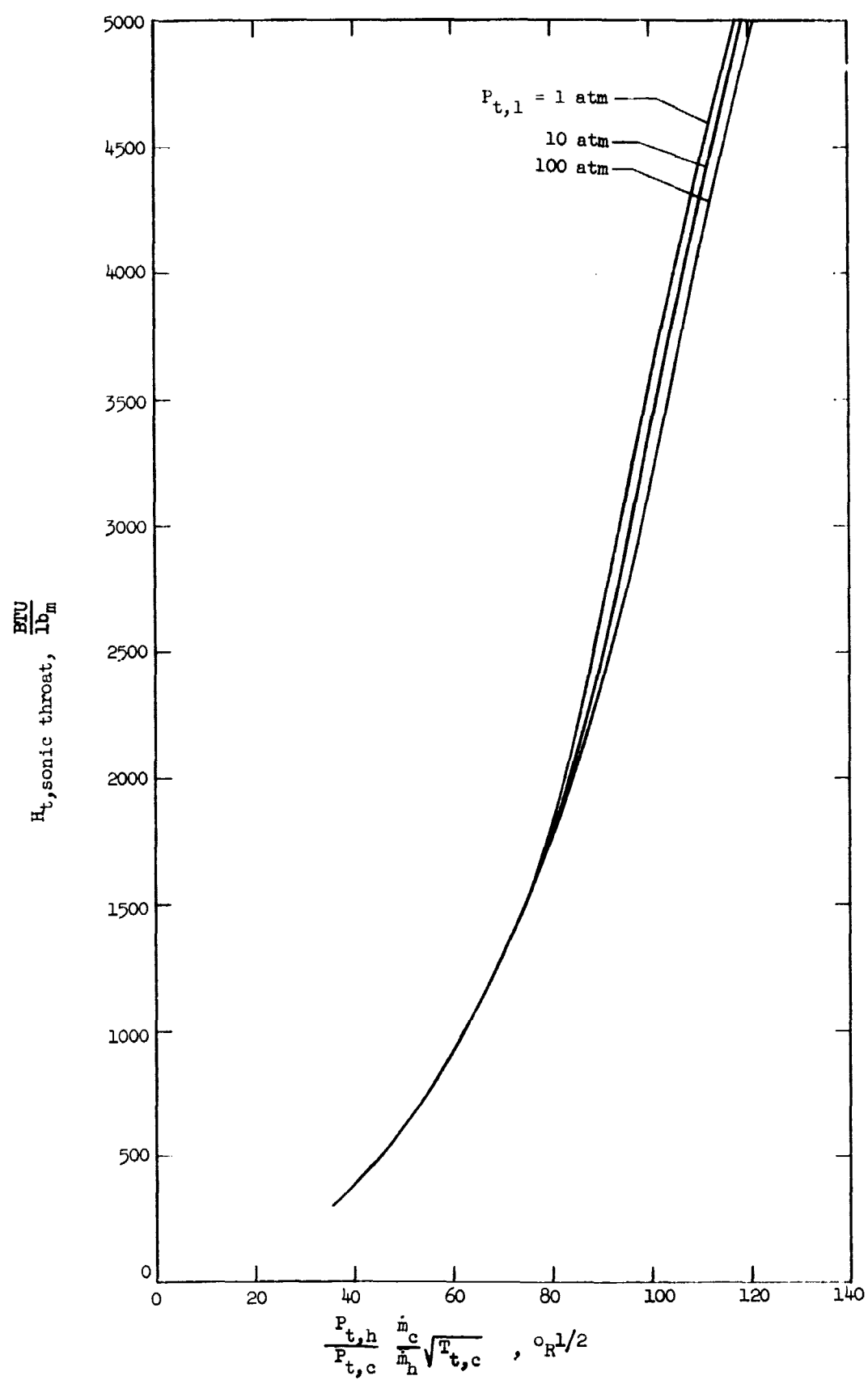


Figure 5.- Curves for the determination of total enthalpy by the equilibrium sonic-throat method.

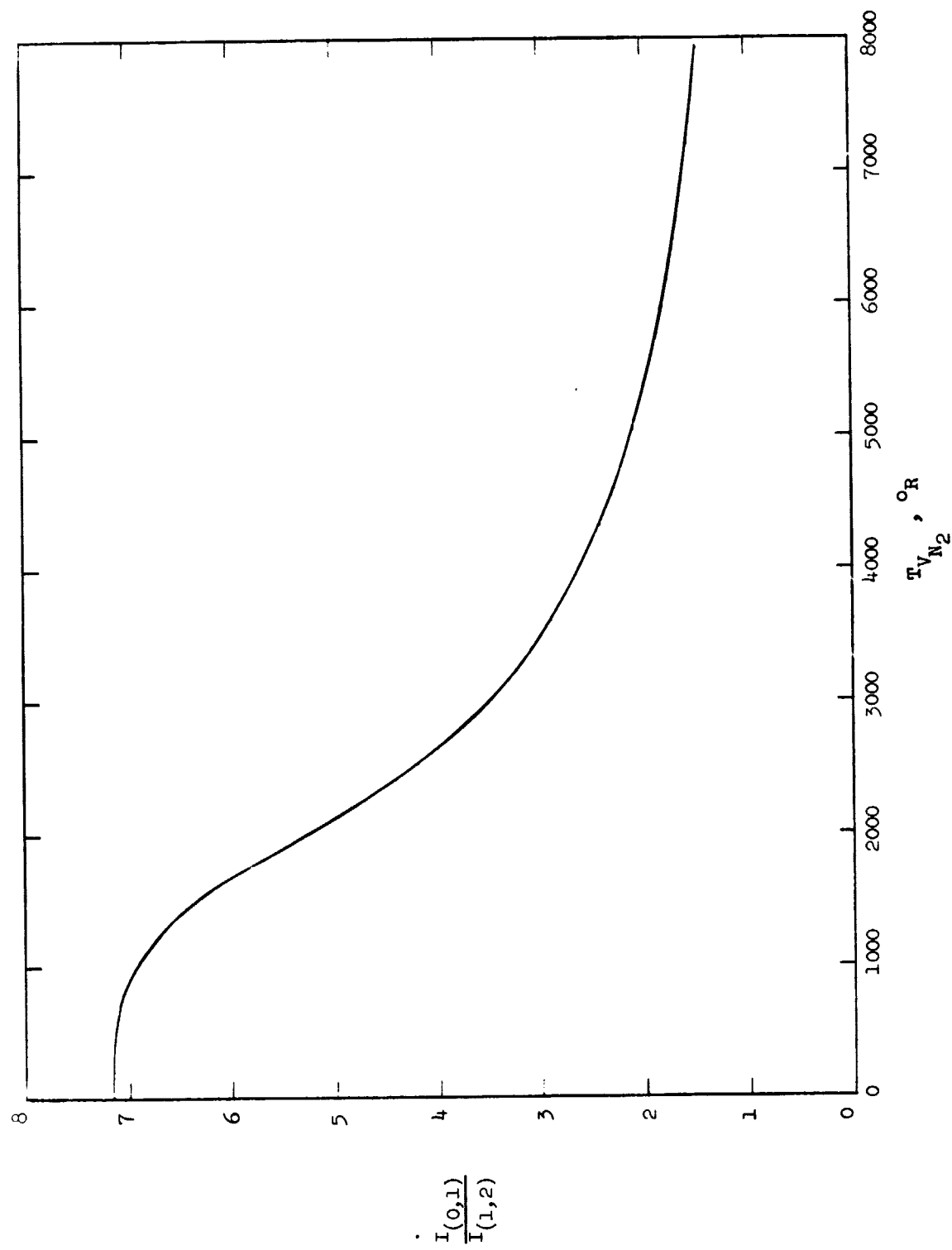


Figure 6.- Ratio of the relative intensities of the (0,1) and (1,2) vibrational bands of electron-beam excited N_2^+ as a function of vibrational temperature of N_2 .

Test 45

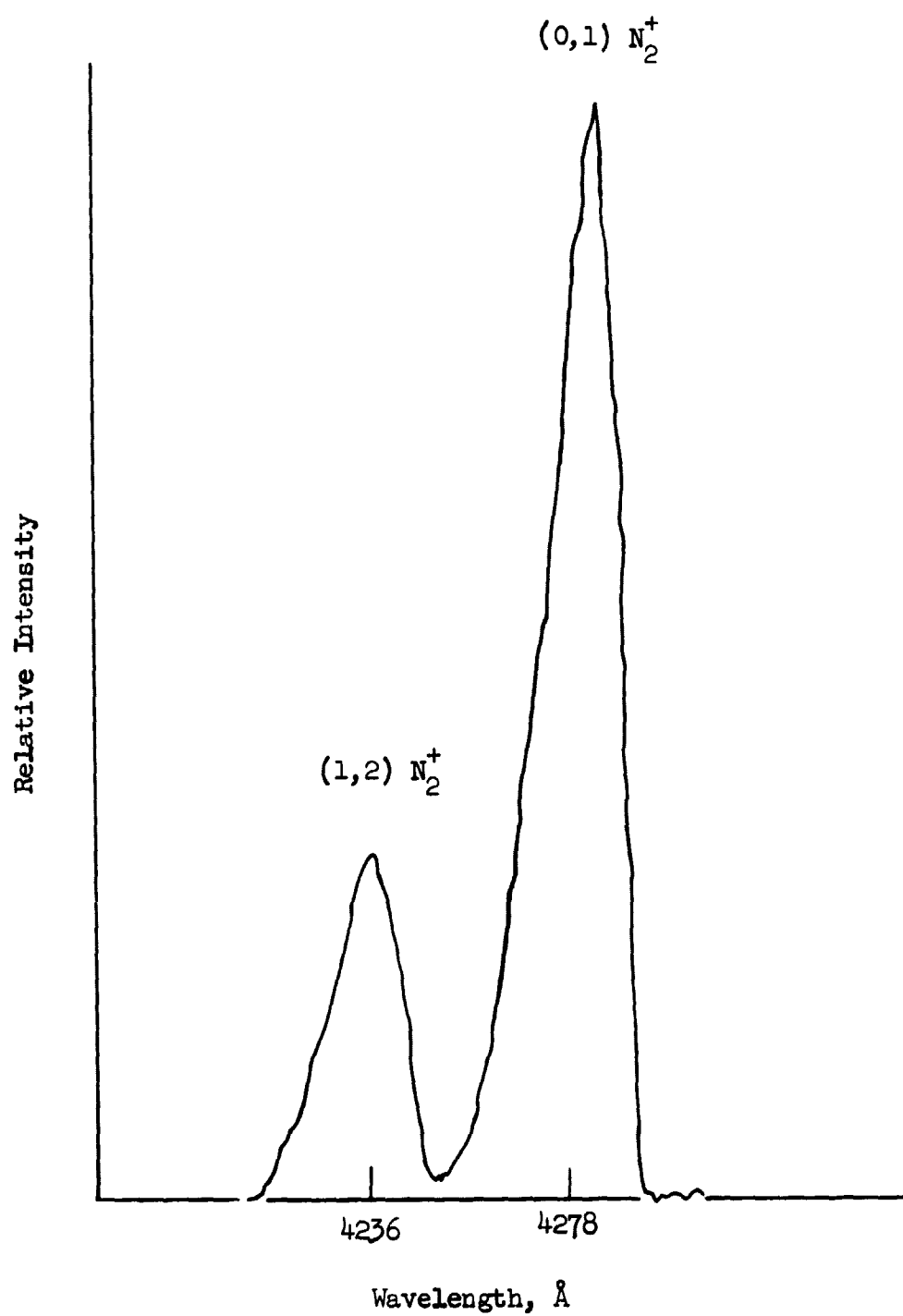


Figure 7.- A typical spectrometer record of the relative intensities of the (0,1) and (1,2) vibrational bands of electron-beam excited N₂⁺.

Rotational Temperature

The relative intensities of the rotational lines of the R-branch of the (0,0) vibrational band of N_2^+ were used in the determination of the rotational temperature. A typical spectrometer scan of the rotational lines within this band is shown in Figure 8.

The most commonly used model for calculating rotational temperature from the measured relative intensities is that of Muntz (Ref. 24). The intensities of the rotational lines according to this excitation-de-excitation model can be expressed as

$$\frac{I_{K',K''}}{K'G\nu_{K',K''}^4} = e^{-K'(K'+1)\theta_{ROT}/T_R} \quad (2)$$

The rotational temperature can be obtained by plotting $\ln [I_{K',K''}/K'G\nu_{K',K''}^4]$ against $K'(K'+1)$. $\nu_{K',K''}$ is the wave number and is very nearly constant for the band. G is a function of K' and T_R and therefore the solution for T_R is iterative. The slope of the straight line on the intensity plot is θ_{ROT}/T_R where θ_{ROT} for N_2 is $2.891^\circ K$.

Several problems are often encountered when attempting to reduce the intensity data from the spectrometer. Ashkenas (Ref. 25) presents a summary of these problems along with a critical review of data reduction techniques. Some of these problems are:

- (1) Overlap of the P-branch onto the R-branch of the (0,0) band of N_2^+ with possible incorrect intensity values.
- (2) Poor resolution of rotational lines resulting in incorrect intensity values.

Test 57

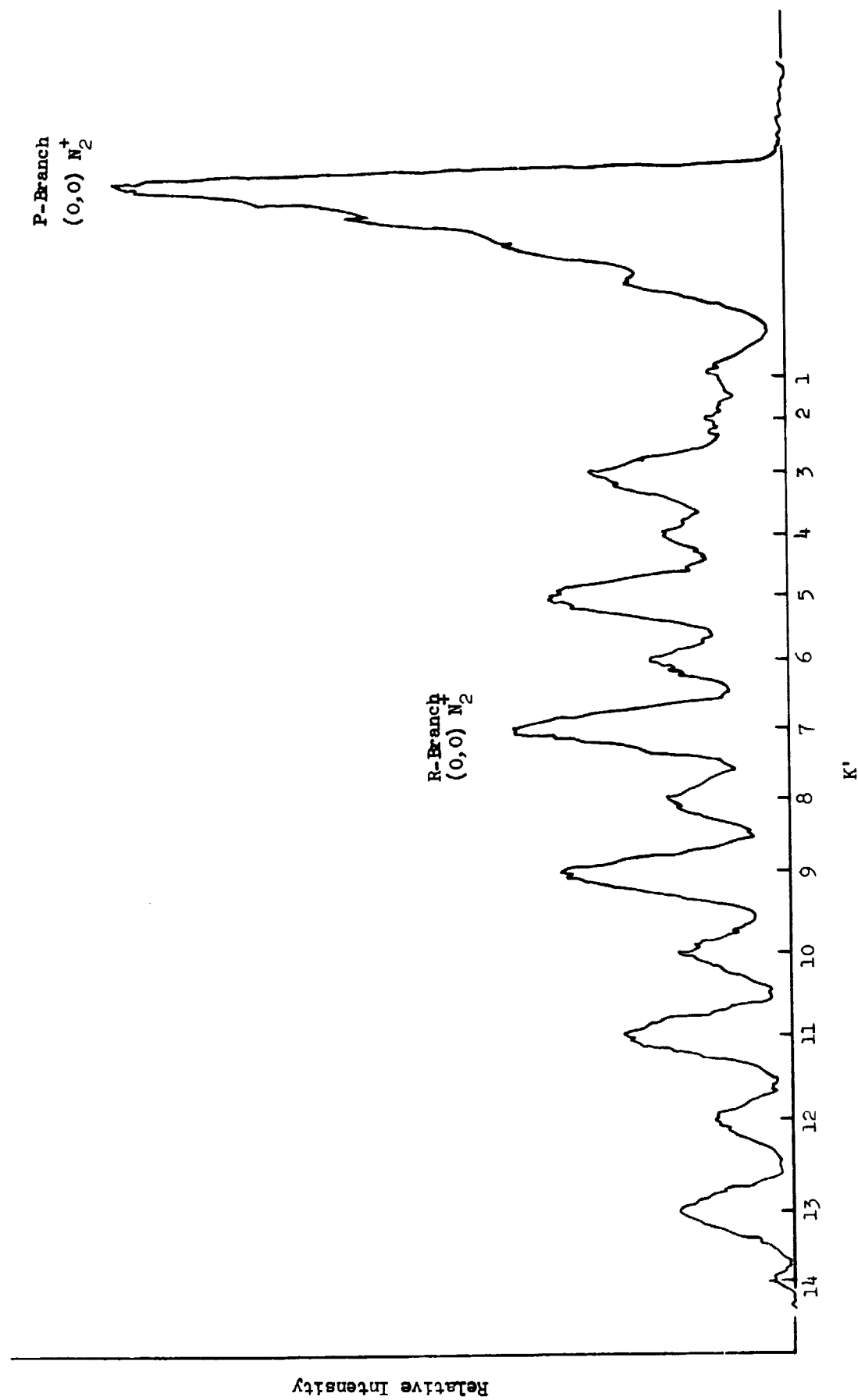


Figure 8.- A typical spectrometer record of the rotational lines of the (0,0) vibrational band of electron-beam excited N_2^+ .

(3) Overlap of other bands, limiting the number of useful rotational lines.

(4) Beam current and/or density variations during the spectrum scan, resulting in erroneous intensity values.

(5) Failure of the measured intensity values to define a straight line when plotted, as mentioned above.

As noted by Ashkenas, (1) and (3) pose no serious threat to the method; (2) is a function of signal strength and type of spectrometer and is not a serious problem at higher rotational quantum numbers; (4) may be avoided by careful monitoring during the test; (5) non-linearity of the data poses a limitation on the technique and does not seem to have been resolved satisfactorily in the literature.

In most research investigations, the higher rotational levels seem to be overpopulated, thus producing the nonlinear effect. The possibility of not being able to define a rotational temperature then arises. According to Reference 25, if the gas is in thermodynamic equilibrium with no overlapping, all measured spectral lines must fall on a straight line on the intensity plot. If this does not occur, then the excitation-de-excitation model must be questioned.

Another problem that arises with the Muntz model is the consistent overprediction of the true temperature; that is, the predicted values are higher than are obtained from other methods (thermocouples, inference from pitot pressure in flowing systems, etc.). This problem becomes much worse at lower temperatures.

As mentioned previously, both of these problems are discussed in the literature, and various solutions are proposed and reasons hypothesized. Robben and Talbot (Ref. 26) encountered both problems (i.e., nonlinearity of the intensity curve and the overprediction of rotational temperature by the Muntz model). These authors suspected that secondary electrons could be the cause of the problem. They presented a rotational temperature correction curve based on their data obtained in nozzles and free jets.

Marrone (Ref. 27), based on his own free-jet experiments, contended that the high temperatures encountered by Robben and Talbot (Ref. 26) could be due to rotational freezing, although he, too, recognized secondary electrons as a possible cause. He also encountered the nonlinearity problem and questioned whether it might be due to rotational freezing or to secondary electrons. Tirumalesa (Ref. 28) concluded that the high temperatures can be explained by rotational freezing.

Hickman (Ref. 29) suggested that the model proposed by Muntz was incorrect, and he presented a new model for the reduction of rotational temperature data. This new model allows rotational changes of $\Delta K = \pm 1$ and ± 3 as opposed to the Muntz model which only allows $\Delta K = \pm 1$. According to Hickman, his model will give accuracy to within the magnitude of the characteristic rotational temperature of N_2 . Data reduction according to Hickman's model also utilizes Equation (2), but with a different expression for G .

Ashkenas (Ref. 25) compared Muntz's and Hickman's models with thermocouple data obtained in a near-static gas at 144° R and 540° R for a range of densities. He reports similar shortcomings of both models, although Hickman's model does give lower temperatures. Ashkenas found that a rotational temperature measurement is dependent on the density and on the number of spectral peaks used in an analysis. Limited corrections (near 144° and 540° R) could be made to rotational temperature data on the basis of Ashkenas' work; however, some degree of scatter is evident in the correlations that would have to be used.

Lillicrap (Ref. 30) noted that the model used by Muntz predicts rotational temperatures that are too high and suggested secondary electrons as the cause since they will not necessarily obey the optical selection rules. He successfully reduced the data of Ashkenas (Ref. 25) with a formulation including the effects of secondary electrons. However, the application as presented is essentially limited to the data of Ashkenas.

Because of the uncertainties involved in obtaining rotational temperature from the intensity data, the experimental data was reduced using both models. However, on the basis of Ashkenas' work (Ref. 25), Hickman's model should give the best results in the density range of the present tests.

In reducing the data, any spectral line intensities that were suspected of being affected by poor resolution, overlap of the P-branch, or electronic noise were omitted. This generally meant not using the first two and the last two spectral lines appearing in the band. The

scatter and nonlinearity of the remaining points was reasonable and a straight-line fit was made to this data on an intensity plot.

A typical rotational temperature data reduction plot is shown in Figure 9. These data points are from the spectrometer trace shown in Figure 8. The faired line is from a computer program modeled after that of Hickman (Ref. 29) which was used to check the data reduction results. This program uses a least squares fit to the data and iterates seven times to insure convergence of the iteration process.

Wall Static Pressure

A nozzle distribution of pressure measurements was not taken due to the 5-1/2-foot length of the shallow 5° half-angle nozzle. Two static pressure orifices were used; one was located directly above the pitot probe tip and the other was located ahead of the tip as a check on source flow effects. Readings from these two orifices generally agreed within 3 per cent or less.

Many investigators have used slender ogive-cylinder probes with orifices located well back from the tip to determine free-stream static pressure (Refs. 1, 2, 3, and 4). This technique involves a calculation of the effects of boundary-layer-induced pressure (Ref. 31) in the measured pressure.

Also, in high-temperature, low-density flows, thermal transpiration (Ref. 32) and the heat-transfer orifice effect (Refs. 33 and 34) may influence the pressure measurement. All of these factors must be considered for tests in the 1-foot hypersonic arc tunnel.

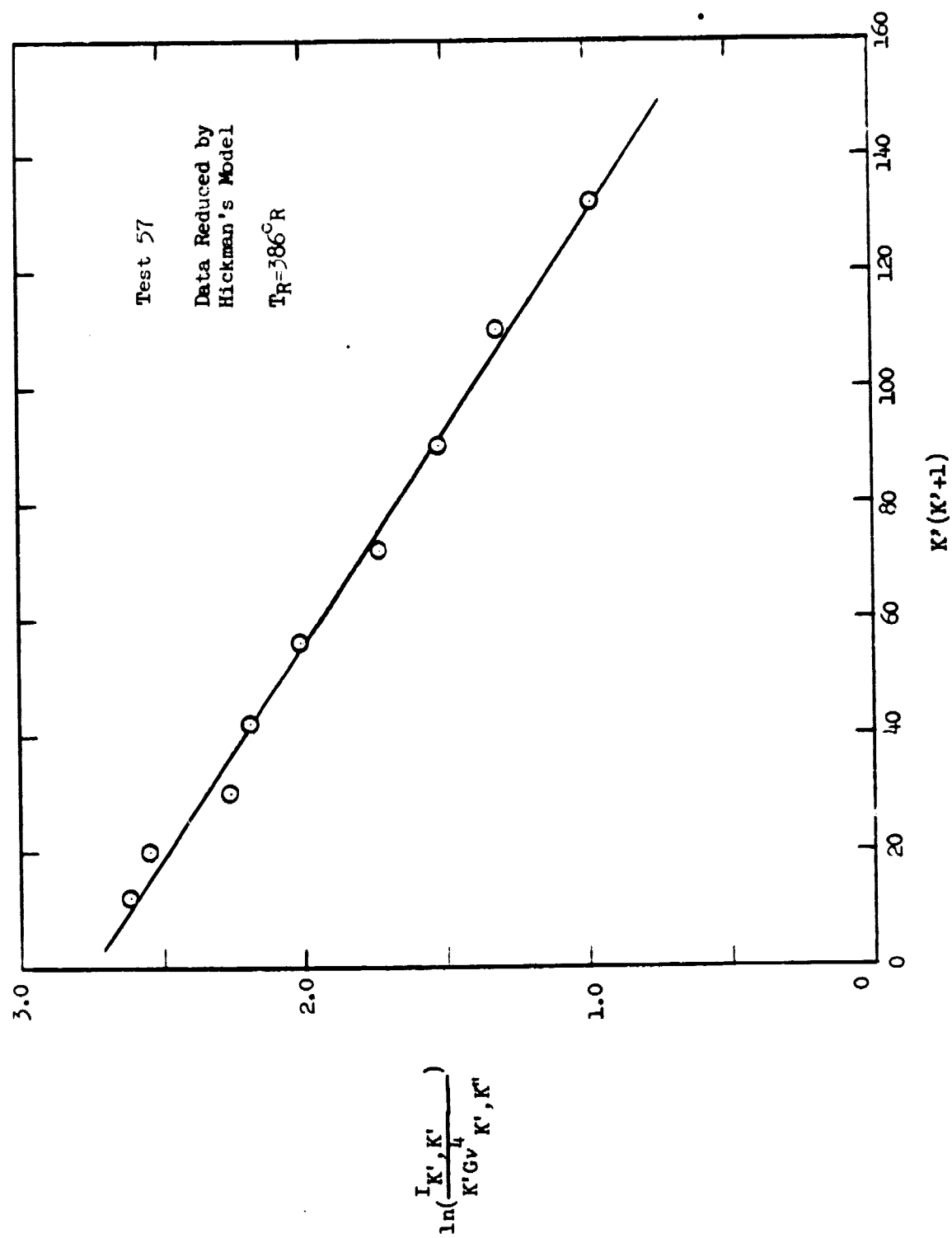


Figure 9.- Variation of $\log_e(I/K'\nu^4G)$ with $K'(K' + 1)$ for the (0,0) vibrational band of N_2 to determine the free-stream rotational temperature of N_2 .

Several difficulties also arise when using nozzle wall pressures as a diagnostic technique. One problem is concerned with taking measurements in the low-density regions. As the boundary layer along the nozzle grows, a contouring effect occurs. This is illustrated in Figure 10, where the equilibrium boundary-layer growth for three different enthalpies is shown. These theoretical data were taken from an existing program. The wall static pressures may be increased in the low-density regions by weak compression waves created by the boundary-layer contouring. Petrie (Ref. 5) and others have noted a relative increase in wall static pressure as the low-density regions were reached. MacDermott and Marshall (Ref. 7) measured wall static pressures that were higher than theory and corrected their data by equating wall pressure to pressure at the edge of the boundary layer and relating the pressure at this location to that at the nozzle centerline by use of measured pitot profiles and assumed isentropic flow in the core. No such corrections were made to the present data, since such a correction technique requires a better definition of core size than was apparent from the pitot surveys (Fig. 11).

A correction was made to the pressure data for the heat-transfer orifice effect. This phenomenon involves an erroneous low pressure indication due to orifice size in a low-density flow with heat transfer. In the present tests, upward corrections to the measured data ranged from 3 per cent at the lowest enthalpy to 12 per cent at the highest enthalpy. Thermal transpiration effects were not important since the wall temperature was the same as the gauge temperature.

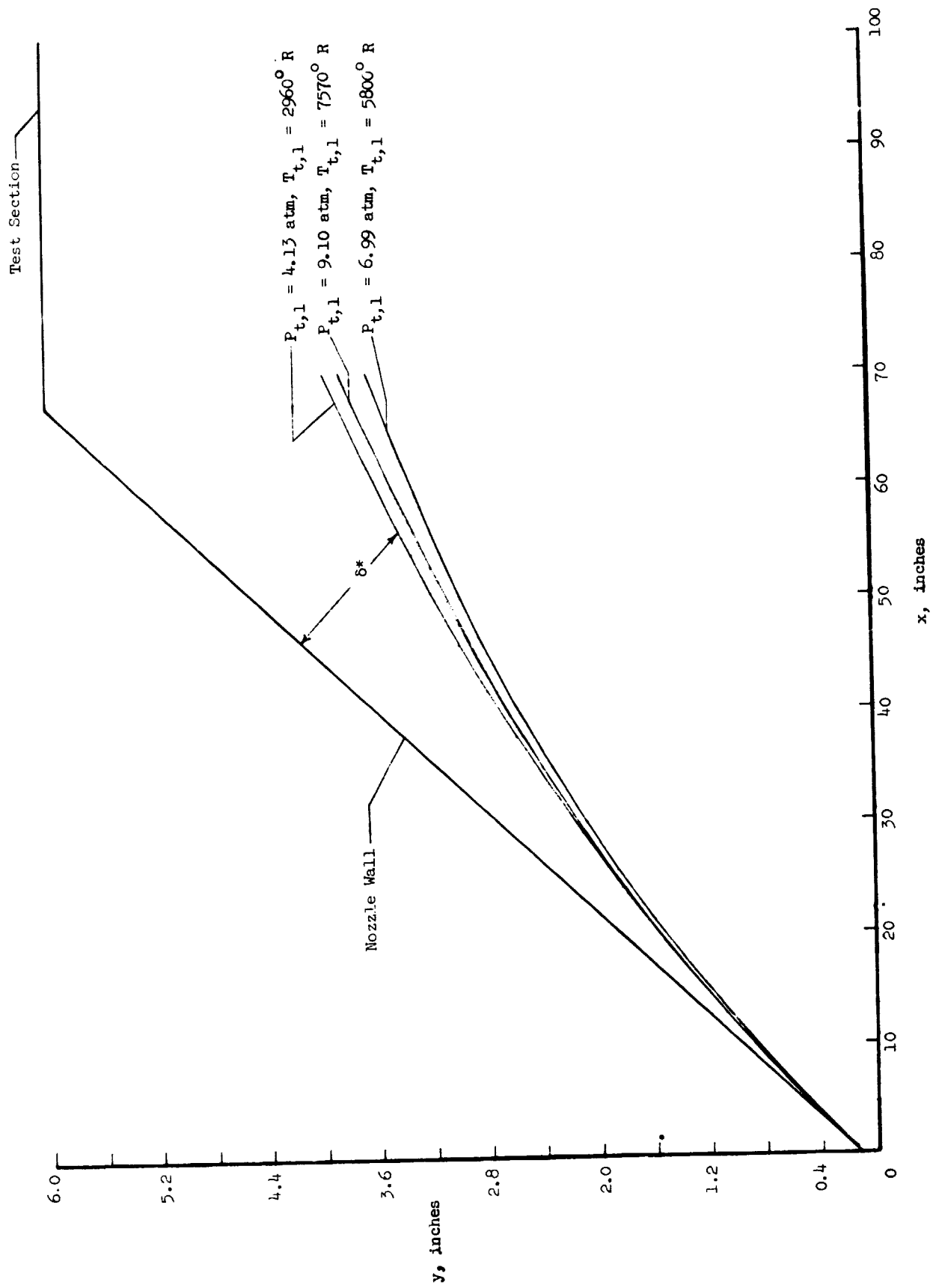


Figure 10.- Examples of boundary-layer contouring for an equilibrium expansion in a 5° half-angle conical nozzle ($d^* = 0.212 \text{ inch}$).

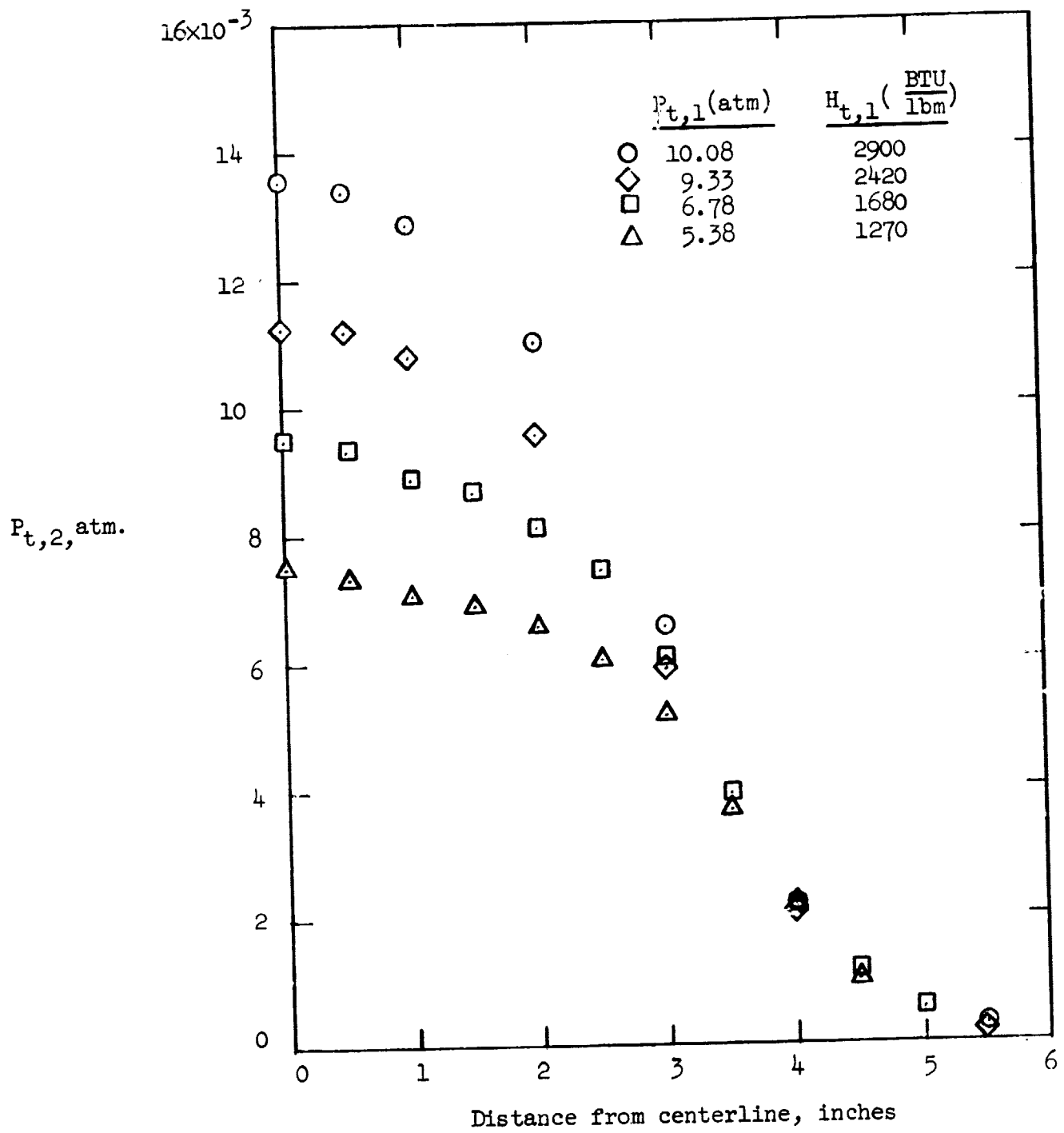


Figure 11.- Pitot pressure surveys across the test section for a range of test conditions (surveys taken 2-1/4 inches from nozzle exit).

Pitot Pressure

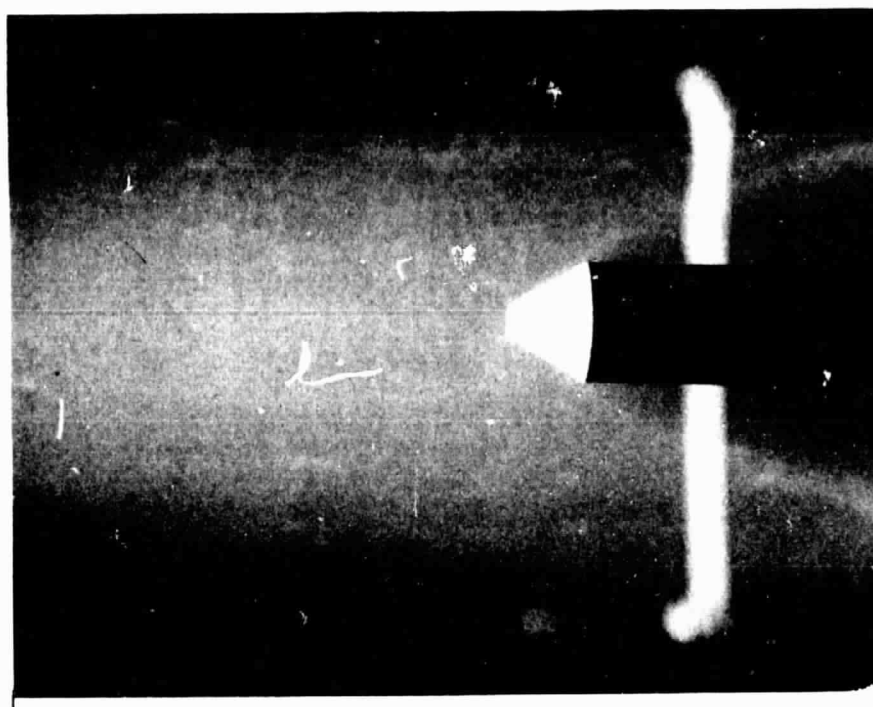
Pitot pressure data were readily reduced except for a second-order viscous effect in the merged layer regime. Corrections for the viscous effect on pitot pressure found in References 35 and 36 indicated that this correction was less than 2 per cent and therefore should be neglected. Agreement between probes ranging from 1/4-inch diameter to 1-inch diameter also supported the neglecting of the viscous correction.

Density and Velocity

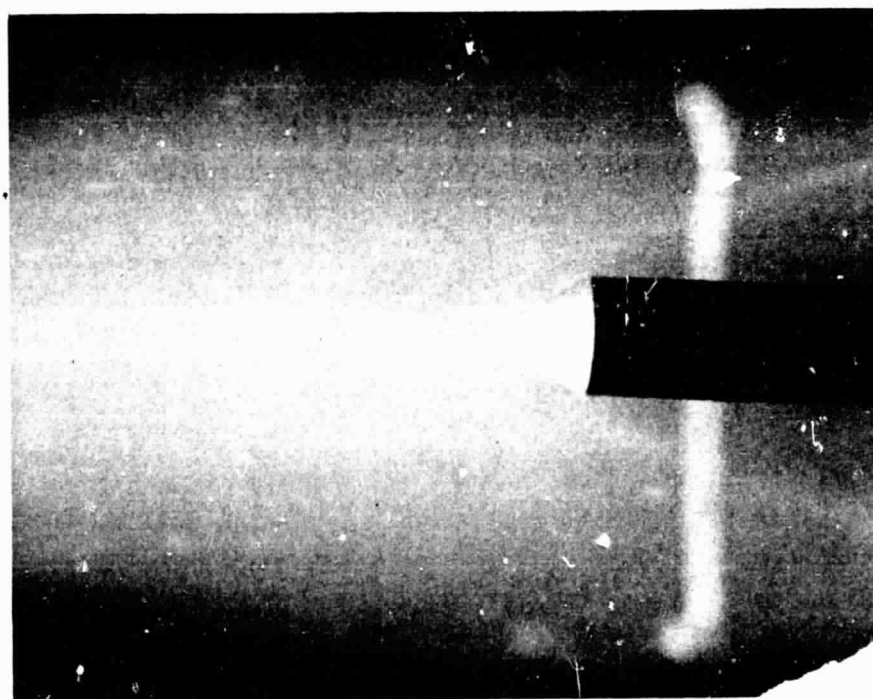
The data obtained from the mass flow probe were probe mass flow rate (with the valve open) and pitot pressure (with the valve closed). The probe mass flow rate is equal to the product of free-stream density and velocity and the entrance area of the probe, that is,

$$\dot{m}_p = \rho_\infty V_\infty A_p \quad (3)$$

if the shock is swallowed so that the cross-sectional area of the swallowed stream tube is equal to the geometric area of the probe entrance. The equal interior and exterior angles of the tip were designed to achieve this. It is difficult to prove that the probe swallowed the shock; however, photographs of the probe tip with the valve closed and with the valve open (Fig. 12) appear to indicate that the shock is swallowed. The self-luminescence of the flow made the shock visible. Note the presence of the gas cap with the valve closed



(a) Valve open.



(b) Valve closed.

Figure 12.- Photographs of the mass flow probe tip illustrating the disappearance of the stagnation region gas cap when applying a very low downstream pressure to the probe.

and its absence when the valve is open. When the valve was slowly opened, the slow recession of the gas cap into the probe could be observed. The only other proof of the swallowing of the shock is an indirect proof by the comparison of measured density and velocity with theory.

No corrections were necessary to the value of probe mass flow rate obtained from the sonic orifice. Probe centerline gas temperatures upstream of the orifice indicated that the flow was cooled to the same temperature at which the orifice was calibrated. Thus, with a knowledge of the probe flow rate and the entrance area ($d = 0.240$ in.), the product of free-stream density and velocity was obtained from Equation (3).

In hypersonic flow, the pitot pressure may be closely approximated by the product of free-stream density and free-stream velocity squared, that is,

$$P_{t,2} = B \rho_{\infty} V_{\infty}^2 \quad (4)$$

The factor B is very weakly dependent on the ratio of specific heats and, consequently, is weakly dependent on the particular gas model chosen (equilibrium, nonequilibrium, or frozen). The equation

$$P_{t,2} = 0.925 \rho_{\infty} V_{\infty}^2 \quad (5)$$

was used since the approximate gas model was known from the rotational temperature measurements.

Comparisons of the pitot measurements from the mass flow with the pitot measurements from the geometrically similar probe with $d/D = 0.333$ indicated as much as a 3 per cent upward correction to the pitot pressure obtained from the mass flow probe. Thus, the pitot pressure measured by the mass flow probe was relatively unaffected by pressure bleed-off effects.

Equations (3) and (5) may be combined to obtain the expression for free-stream velocity as follows:

$$V_{\infty} = \frac{P_{t,2}}{0.925} \frac{A_p}{\dot{m}_p} \quad (6)$$

Free-stream density may be calculated by inserting this value of V_{∞} into Equation (3).

Stagnation Point Heat Transfer

In order to reduce the heat-transfer data, an effective radius of the hemisphere was required since the body radius was 0.5 inch and the nose radius was 1 inch (not a true hemisphere). The probe was originally intended to have a 1-inch-diameter hemispherical tip; however, installation of the constantan disk blunted the tip. The true shape of the probe was determined by a 10 power magnification on an optical comparator. The actual shape of the probe is shown in Figure 13 by the solid lines.

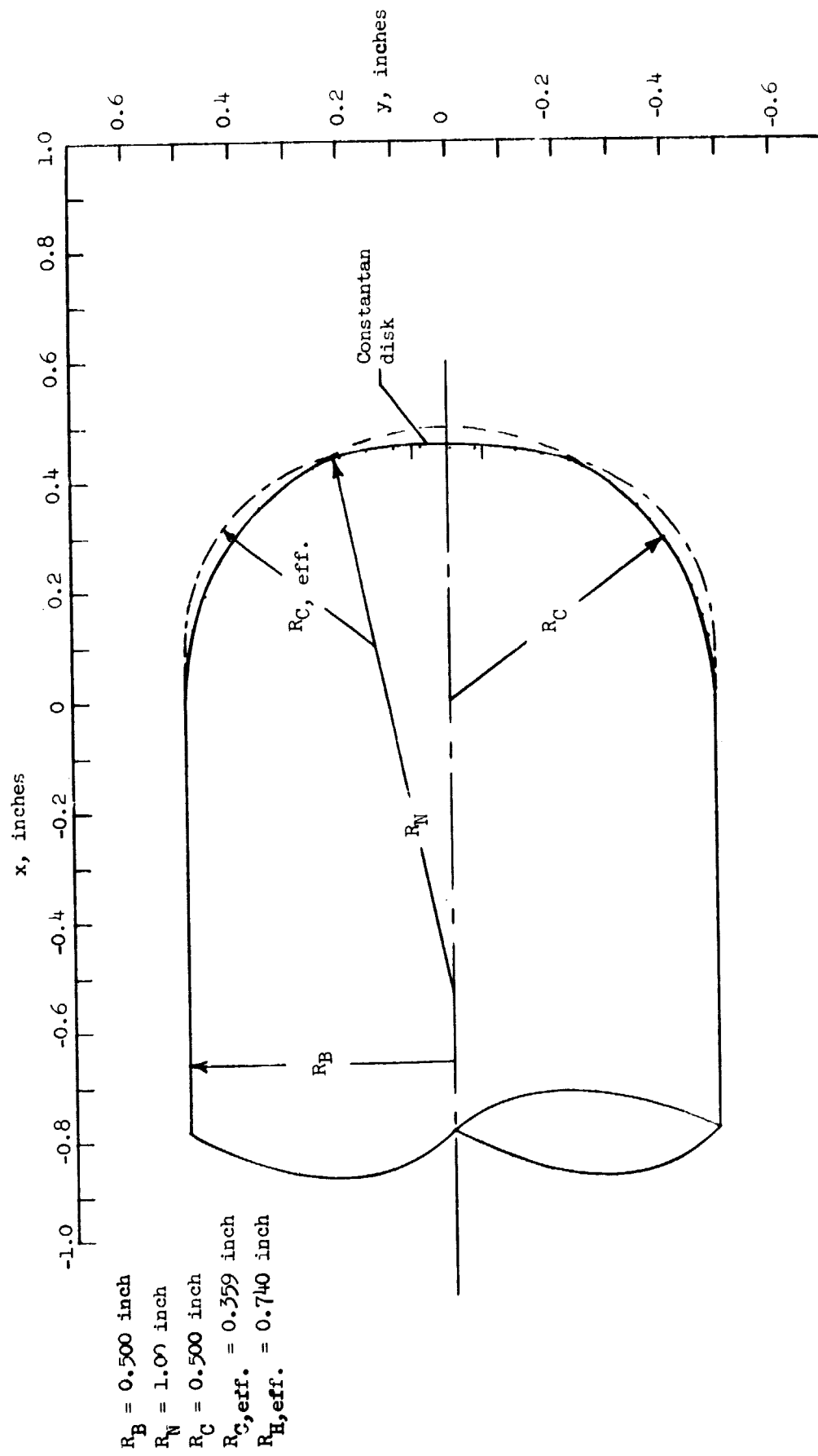


Figure 13.- Actual shape of the tip of the stagnation point heat-transfer probe and the shapes used to define the limits of the effective hemisphere.

References 37, 38, and 39 present data on stagnation-point velocity gradients for nose shapes varying from hemispheres to flat-faced probes. Using these velocity gradients, a particular shape can be simulated by a hemisphere with an effective radius. $R_{H,eff}$ is a function of nose radius, body radius, and corner radius. For all of these studies, the center of the corner radius was located on the radius arm of the nose radius at the intersection point of the two arcs; that is, the corner arc and the nose arc had the same slope at the point of intersection.

A region of rapidly changing curvature formed the transition from the nose radius of curvature to the corner radius of curvature in the present case. To this author's knowledge, no information on stagnation-point velocity gradients on this type of configuration is available. Thus, an effort was made to form reasonable estimates of the limits of the effective radius from the data presented in Reference 39.

The first obvious limit on $R_{H,eff}$ is that it can be no less than the radius of the original hemisphere, that is, $R_{H,eff} > 1/2$ inch. The other limit is more difficult to determine. The effective corner radius which would be tangent to the nose arc at the intersection with the original corner radius was determined graphically. The other constraint on this effective corner radius was that it become tangent to the 1-inch-diameter cylindrical afterbody extended. The effective corner radius was found to be 0.359 inch.

This new body now was of the same class studied in Reference 39. Thus, another limit for the effective hemispherical radius was found from this reference as a function of nose radius, effective corner radius, and body diameter. $R_{H,eff}$ was determined to be 0.740 inch. Thus,

$$0.500 < R_{H,eff} < 0.740$$

are the limits (in inches) on the effective hemispherical nose radius. These are still rather broad limits and restrict the ability to compare the heat-transfer data with theory. However, the stagnation point heat-transfer rate is inversely proportional to the square root of the hemisphere radius and, therefore, the uncertainty in heat-transfer rate is considerably less than the uncertainty in the radius.

CHAPTER IV

THEORY

Enthalpy Determination

Plenum chamber.- The total enthalpy at the exit of the plenum chamber was measured using the total calorimeter. The enthalpy at this point was also determined theoretically by use of the equilibrium sonic-throat method. The validity of the sonic-throat method depends upon a knowledge of the thermochemical state of the gas in flowing from the plenum chamber to the throat as well as a knowledge of the effective throat area. The theory of the sonic-throat technique, including some factors which may affect the method, is covered extensively in Reference 21. Reference 22 also provides good coverage of the method.

Only the equilibrium sonic-throat method will be considered here, since the technique was used as a correlation tool in the present tests. The equations for the steady, isentropic, one-dimensional flow of a gas through the nozzle are

$$\text{Continuity} \quad \dot{m} = \rho AV \quad (7)$$

$$\text{Energy} \quad H_{t,1} = h + \frac{V^2}{2} \quad (8)$$

$$\text{State} \quad P = Z\rho R_s T \quad (9)$$

At the nozzle throat,

$$\dot{m} = \rho^* A^* V^* \quad (10)$$

Combining Equations (8), (9), and (10), one obtains

$$\frac{\dot{m}}{A^* P_{t,1}} = \frac{\sqrt{H_{t,1}}}{Z_{t,1} R_s T_{t,1}} \left(\frac{\rho^*}{\rho_{t,1}} \right) \sqrt{2 \left(1 - \frac{h^*}{H_{t,1}} \right)} \quad (11)$$

For a perfect gas, this reduces to ($Z_{t,1} = 1$):

$$\frac{\dot{m}}{A^* P_{t,1}} = \frac{1}{\sqrt{H_{t,1}}} \sqrt{\frac{\gamma^2}{\gamma - 1} \left(\frac{2}{\gamma + 1} \right)^{\gamma+1/\gamma-1}} \quad (12)$$

and the dependence of total enthalpy on mass flow rate, effective area ratio, and plenum chamber pressure is noted.

Winovich (Ref. 21) derives expressions from the general equation, (11), for a perfect gas, a calorically perfect gas, and a real gas. However, in the present case, plots of $\frac{P_{t,h}}{P_{t,c}} \frac{\dot{m}_c}{\dot{m}_h} \sqrt{T_{t,c}}$ versus $H_{t,1}$ were used for the sonic-throat method (Fig. 5). The values of $\frac{P_{t,h}}{P_{t,c}} \frac{\dot{m}_c}{\dot{m}_h} \sqrt{T_{t,c}}$ were obtained from the equilibrium throat conditions of the Cornell Aeronautical Laboratory computer program (Ref. 12) by using the assumption that $A_{eff,c}^* = A_{eff,h}^*$.

Test section.- The enthalpy in the test section of the wind tunnel is the same as that in the plenum chamber if the gas has expanded adiabatically through the nozzle. This assumption is commonly made, although it should be checked in an arc-heated wind tunnel. Probably the best technique for determining the total enthalpy in the test section is the shock-swallowing enthalpy probe with separate cooling passages for the internal and external coolant flow. However, in the absence of such a probe, the stagnation point heating rate is often

used to infer the enthalpy. This is accomplished by relying on a theoretical or empirical relation involving the heat-transfer rate and the total enthalpy. For example, Zoby (Ref. 40) presents the following empirical formula for stagnation point heat transfer to a hemisphere in air.

$$\dot{q} \sqrt{\frac{R_H}{P_{t,2}}} = 0.0461(H_{t,1} - h_w) \quad (13)$$

where \dot{q} is in Btu/ft²-sec, R_H is in feet, $P_{t,2}$ is in atmospheres, and $H_{t,1}$ and h_w are in Btu/lbm. This equation inherently assumes a fully catalytic wall with a Lewis number of unity.

In low-density, high-enthalpy flows, one must exercise extreme care in using the stagnation point heat-transfer rate to determine total enthalpy. Two problems which affect the measured heat-transfer rates are the catalytic efficiency of the gauge surface and second-order viscous effects. If the stagnation point boundary layer were in equilibrium and viscous effects small, the data would still be useful for calculating total enthalpy. In any event, it is appropriate to determine what conclusions can be drawn from the data, even with the uncertainty in effective radius.

Rosner (Ref. 41) presents an equation for stagnation point heat transfer to a hemisphere, including the effects of varying degree of wall catalycity. This equation is identical to the frozen boundary-layer equation of Fay and Riddell (Ref. 42) with the exception of the term involving the wall catalycity. This equation is

$$\dot{q} = 0.763 \left(\frac{\rho_w \mu_w}{\rho_e \mu_e} \right)^{0.1} (\beta \rho_e \mu_e)^{0.5} (\text{Pr})^{-0.6} \Delta h \left\{ 1 + \phi \left[(\text{Le})^{0.6} - 1 \right] \frac{\Delta h_{\text{chem,max}}}{\Delta h} \right\} \quad (14)$$

where

$$\Delta h = (H_{t,1} - h_{f,w}) - (1 - \phi) \Delta h_{\text{chem,max}} \quad (15)$$

$$\phi = \frac{\alpha_e - \alpha_w}{\alpha_e} = \frac{1}{1 + \frac{S}{K_w}} \quad (\text{for a completely frozen boundary layer}) \quad (16)$$

$$S = 0.763 (\beta \rho_e \mu_e)^{0.5} (\text{Sc})^{-0.6} \rho_w^{-1} \quad (17)$$

$$\beta = \frac{V_\infty}{R_H} \left[\frac{\rho_\infty}{\rho_2} \left(2 - \frac{\rho_\infty}{\rho_2} \right) \right]^{0.5} \quad (18)$$

In the preceding equations, the extent of recombination, ϕ , contributes perhaps the most uncertainty to the calculated value of heat transfer. If both the shock layer and the boundary layer are in a state of nonequilibrium, the calculation of ϕ becomes a monumental task. If conditions at the edge of the boundary layer are known and if the boundary layer is frozen, ϕ may be expressed in terms of the surface catalytic reaction rate constant, K_w , and the quantity S , which is a measure of the diffusion velocity in the boundary layer. Even in this case, K_w is a relatively uncertain factor. K_w for cupric oxide was calculated for use with the present tests, using data from Reference 43; however, extreme caution must be exercised in using values in the literature (Carden, Ref. 44) since surface catalytic

properties of metals are dependent on surface preparation as well as the duration of exposure to atomic specie.

Prior to applying the heat-transfer theory, some knowledge of the state of the gas in the shock layer and in the stagnation point boundary layer is necessary (i.e., Is the gas frozen? In a nonequilibrium state? Or in equilibrium?) This question may be investigated by calculating the Damköhler number which is defined as

$$Da = \frac{\text{Residence time}}{\text{Reaction time}} \quad (19)$$

In the case of the shock layer, the residence time of the fluid is taken to be $2R_H/V_\infty$. Reference 46 presents the following expression for the Damköhler number for chemical dissociation in the shock layer:

$$Da_d = 2K_r \left(\frac{300}{T_f} \right)^\omega \left[\frac{(1 + \alpha)\rho_2}{MW} \right]^2 \frac{(1 - \alpha)}{4P_2} \left[\exp \left(A - \frac{T_D}{T_f} \right) \right] \left[(2 - j) \left(\frac{2R_H}{V_\infty} \right) \right] \quad (20)$$

where T is $^{\circ}K$, ρ_2 is gm/cc, and P_2 is in atmospheres. According to Reference 47, the shock layer is frozen if $Da_d < 3 \times 10^{-2}$. If $Da_d \gg 1$, the shock layer is in equilibrium.

A similar analysis was applied to determine if vibration would be in equilibrium behind the normal shock. In this case, Blackman's relaxation rate equation (Ref. 48) was used for the excitation of the vibrational mode. Thus,

$$Da_v = \frac{\left(\frac{2R_H}{V_\infty}\right) P_2}{\left[1.1 \times 10^{-11} T_2^{1/2}\right] \left[\exp\left(\frac{154}{T_2^{1/3}}\right)\right]} \quad (21)$$

where P_2 is in atmospheres, T_2 is $^{\circ}\text{K}$.

Inger's results (Ref. 49) were used to calculate the state of the boundary layer. The Damköhler number for recombination in the boundary layer is

$$C_1^* = C_1 \alpha_e \left\{ \frac{I_{Z,F_1} + \frac{2L_w}{0.47 Sc^{1/3}} I_{Z,F_2} + \frac{L_w^2}{(0.47 Sc^{1/3})^2} I_{Z,F_3}}{\left(1 + \frac{L_w}{0.47 Sc^{1/3}}\right)^2} \right\} \quad (22)$$

where

$$C_1 = \left[2K_r \left(\frac{300}{T_e}\right) \omega\right] \left[\frac{(1 + \alpha)\rho_e}{MW}\right]^2 \left[\frac{1}{(1 + \beta)\beta}\right] \quad (23)$$

and

$$L_w = \frac{Sc}{\sqrt{\frac{\rho_w \mu_w}{\rho_e \mu_e}}} \left(\frac{K_w}{S}\right) \quad (24)$$

Units and the other parameters, with the exception of I_{Z,F_1} , I_{Z,F_2} , and I_{Z,F_3} , have been previously defined. I_{Z,F_1} , I_{Z,F_2} , and I_{Z,F_3} may be found graphically in Reference 49 as a function of T_w , T_e , T_D , and ω . If $C_1^* < 10^{-1}$, the boundary layer may be considered frozen (Ref. 45).

Low-density, second-order viscous effects may also affect the data. Cheng (Ref. 50) presents a figure showing the ratio $\dot{q}/\dot{q}_{B.L.}$.

versus a Reynolds number defined as $Re_f = \frac{\rho_{t,2} \sqrt{H_{t,1}} R_H}{\mu_{t,2}}$. As the Reynolds number decreases, this ratio increases above 1.0 and then rapidly decreases as free-molecule flow is approached. This figure may be used to obtain a correction to the stagnation point heat-transfer rate in the low Reynolds number regime.

Gas Flow Models

The problem of the nonequilibrium expansion of gas in a nozzle has been investigated for several years. Some of the techniques used will be mentioned briefly, but this by no means lists all of the contributions.

Glowacki (Ref. 9) treated the chemical nonequilibrium behavior of oxygen in a dilute mixture of inert N_2 with vibration assumed to be in equilibrium. Enkerhus (Ref. 10) treated the approximate nonequilibrium case by allowing vibration and chemistry to freeze at a point corresponding to the sudden-freeze point of the oxygen recombination. This amounted to an uncoupled sudden-freeze model for chemistry and vibration. Again, the composition was O_2 and O in a dilute mixture of inert N_2 .

More exact results have been obtained for more complex gas mixtures by the use of electronic computers. Emanuel and Vincenti (Ref. 11) used a model for air consisting of N_2 , N , O_2 , O , and NO which included eight chemical reactions plus the vibrational processes of the three diatomic species. Here, again, however, the chemical and vibrational modes were uncoupled.

Lordi, Mates, and Moselle (Ref. 12) presented a computer program for an air model consisting of N_2 , N, O_2 , O, NO, NO^+ , Ar, and E^- with 11 chemical reactions, although the program can handle 20 species and 64 reactions. Vibration may be assumed either to be in equilibrium with translation and rotation or to be frozen at conditions prior to the expansion.

Tirumalesa (Ref. 13) considered the case of pure oxygen with coupled vibration and dissociation. The coupling models were those of Treanor (Ref. 51).

Dressler, French, and Webb (Ref. 14) developed a computer program for the nonequilibrium flow of air, including nonequilibrium vibrational and electronic energy relaxation and coupling effects between these energy modes and the chemistry. Rotation, vibration, and electronic excitation were considered uncoupled. The program is capable of handling 20 species and 50 reactions.

Thus, it is evident that the available techniques for calculating nonequilibrium flows cover a wide spectrum of exactness and complexity. An excellent survey of nonequilibrium flow is given in Reference 52. This paper notes the status of the problem, both experimental and theoretical.

In the present case, advantage was taken of the ready availability of the program of Lordi, Mates, and Moselle (Ref. 12) for the computation of nonequilibrium chemistry. This program was used in conjunction with a sudden-freeze model of N_2 vibration to predict test section properties. The procedure will be discussed in detail below.

Mention will be made of the limiting cases of nonequilibrium flow in order to present some known bounds to the predicted values of flow properties. Thus, the cases of equilibrium and frozen flow will be considered briefly since the degree of uncertainty in the chemical reaction rates affects the nonequilibrium predictions.

Equilibrium flow.- The basic assumption in equilibrium flow is that all reaction times are zero; that is, the fluid is in complete thermodynamic equilibrium at each stage of the expansion. The assumption of complete thermodynamic equilibrium along with the assumption of a constant entropy expansion makes the calculation of equilibrium flow simple. The specification of one other thermodynamic property and the use of a Mollier diagram enables one to solve the equilibrium expansion for specified plenum chamber conditions.

The equilibrium predictions used in the present investigation were taken from an existing equilibrium flow expansion computer program at Langley Research Center. The species in the simplified equilibrium program are N_2 , O_2 , and O . Results from this program compared favorably with the more complete equilibrium solution (more species included) of the Cornell Aeronautical Laboratory program (Ref. 12). The simpler program was used because entrance to the program was easier since normal shock properties were tabulated.

Nonequilibrium flow.- The nonequilibrium flow solution is much more complicated than the equilibrium solution since finite reaction rates are included. The assumption of constant entropy of the expansion can no longer be made and the history of the flow can no longer be neglected.

The calculation technique of the present study involves using an available chemical nonequilibrium program (rotation, translation, and vibration in equilibrium) for air (Ref. 12) in conjunction with a sudden-freeze criterion for the vibrational mode. The model for air consists of eight species: N_2 , N , O_2 , O , NO , Ar , NO^+ , and E^- . The 11 reactions considered and the forward reaction rate for each are presented in Table I. The program requires a nozzle geometry as input. The actual geometry was a circular arc throat (Radius of curvature = 1.75 inch) followed by a 5° half-angle conical nozzle. The actual nozzle was simulated by fitting a polynomial to the equation of the circular arc throat in the converging throat region. Downstream of the throat, a hyperbolic contour asymptotic to a 5° half-angle cone was used.

The logic involved in computing the nonequilibrium flow is that, in most cases, chemistry will freeze before the vibrational mode freezes during an expansion. (This is not true in the case of atomic nitrogen due to the NO "shuffle" reactions; however, the mass fraction of N was two orders of magnitude lower than other species over the range of conditions of interest here.) Thus, the freezing of both chemistry and vibration at the freezing point of vibration provides a reasonable estimate of fluid properties (including composition) in the test section.

Figures 14(a) and 14(b) show the mass fraction variation of the various species in an expansion down the nozzle. The conditions chosen represent one of the highest enthalpies encountered during

TABLE I.- CHEMICAL REACTIONS USED IN THE NONEQUILIBRIUM
NOZZLE FLOW PROGRAM

Reaction	M	A	η	$E_{act}, \frac{\text{cal}}{\text{mole-}^\circ\text{K}}$
$\text{N}_2 + \text{M} \rightleftharpoons 2\text{N} + \text{M}$	N_2	3×10^{21}	-1.5	-2.2499×10^5
$\text{N}_2 + \text{M} \rightleftharpoons 2\text{N} + \text{M}$	N	1.5×10^{22}	-1.5	-2.2499×10^5
$\text{N}_2 + \text{M} \rightleftharpoons 2\text{N} + \text{M}$	$\text{O}_2, \text{Ar}, \text{O}, \text{NO}$	9.9×10^{20}	-1.5	-2.2499×10^5
$\text{O}_2 + \text{M} \rightleftharpoons 2\text{O} + \text{M}$	O_2	3.6×10^{21}	-1.5	-1.1796×10^5
$\text{O}_2 + \text{M} \rightleftharpoons 2\text{O} + \text{M}$	O	2.1×10^{18}	-0.5	-1.1796×10^5
$\text{O}_2 + \text{M} \rightleftharpoons 2\text{O} + \text{M}$	$\text{N}_2, \text{Ar}, \text{N}, \text{NO}$	1.2×10^{21}	-1.5	-1.1796×10^5
$\text{NO} + \text{M} \rightleftharpoons \text{N} + \text{O} + \text{M}$	$\text{N}_2, \text{O}_2, \text{Ar}, \text{N}, \text{O}, \text{NO}$	5.2×10^{21}	-1.5	-1.4996×10^5
$\text{O}_2 + \text{N} \rightleftharpoons \text{O} + \text{NO}$	---	1.0×10^{12}	0.5	-6.2×10^3
$\text{N}_2 + \text{O} \rightleftharpoons \text{NO} + \text{N}$	---	5×10^{13}	0	-7.552×10^4
$\text{N}_2 + \text{O}_2 \rightleftharpoons \text{NO} + \text{NO}$	---	9.1×10^{24}	-2.5	-1.2912×10^5
$\text{NO}^+ + \text{E}^- \rightleftharpoons \text{N} + \text{O}$	---	1.8×10^{21}	-1.5	0

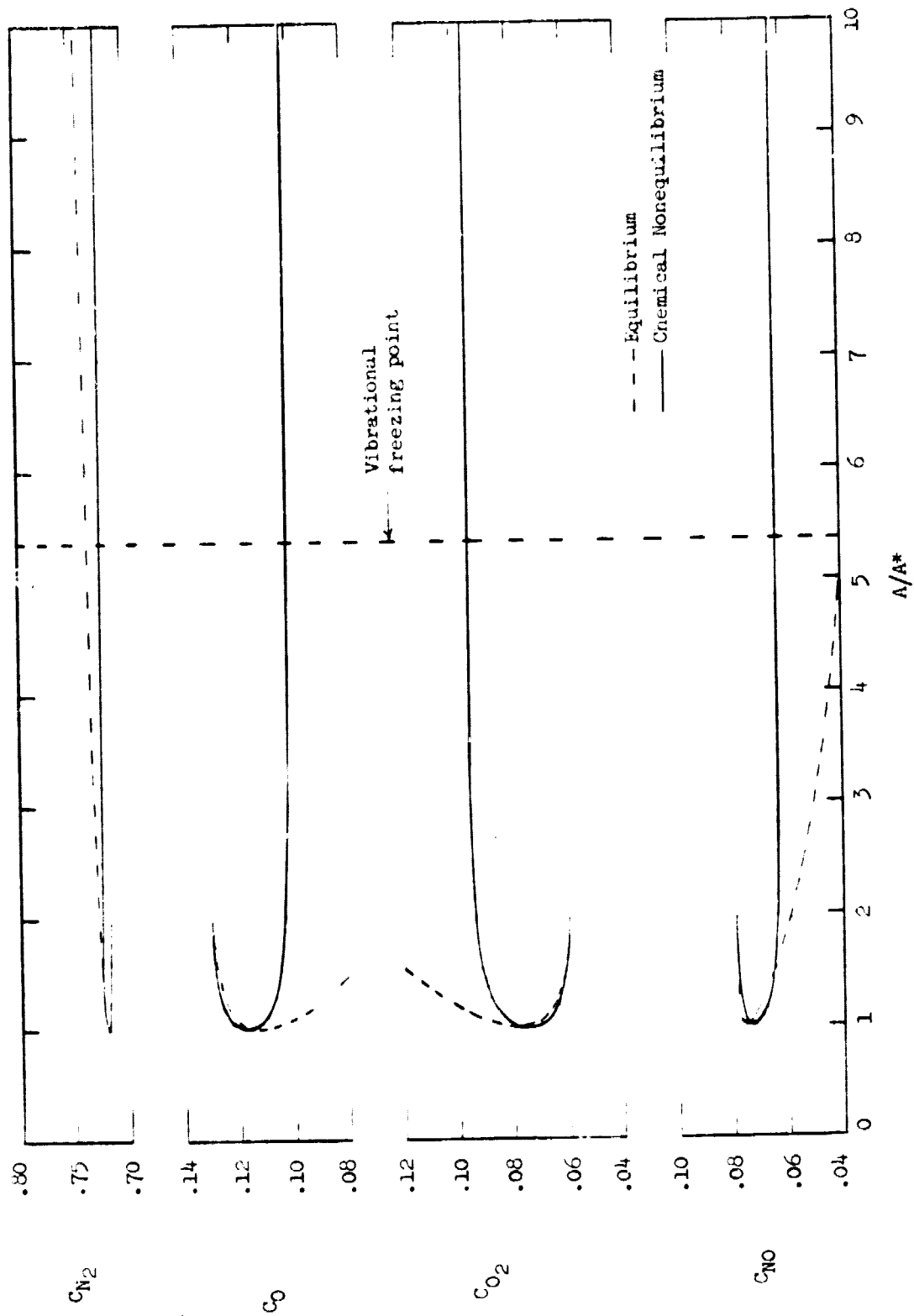
$$K_{F_1} = A_1 T^{\eta_1} \exp \left[\frac{E_{act,1}}{R_u T} \right]$$

where

$$T = ^\circ\text{K}$$

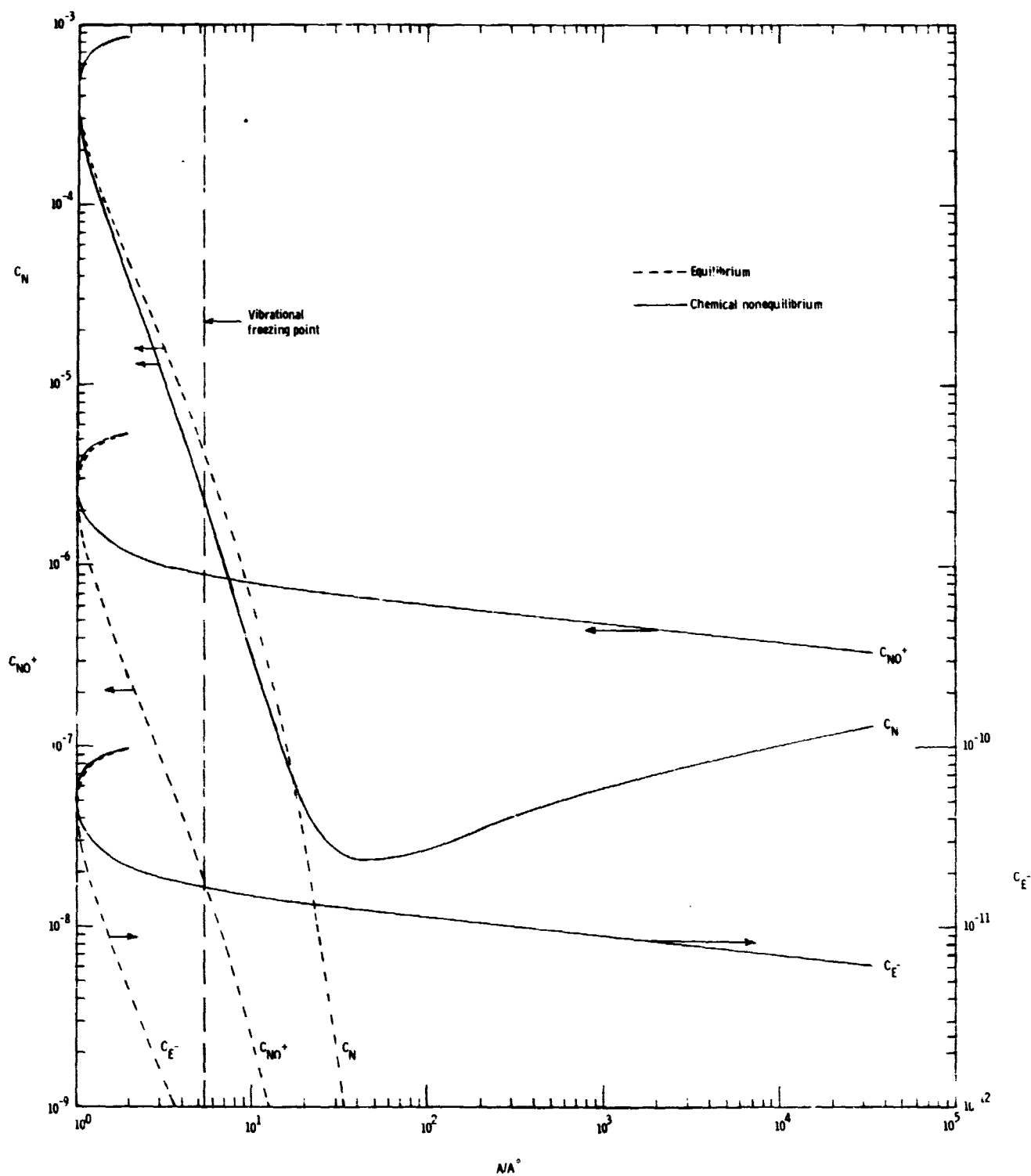
$$R_u = 1.98647 \frac{\text{cal}}{\text{mole-}^\circ\text{K}}$$

$$K_{F_1} = \text{cm}^3/\text{mole-sec}$$



(a) Dominant species ($C_{AR} = 0.0128598 = \text{constant}$).

Figure 14.- Variation of species mass fraction with nozzle area ratio.
($P_{t,1} = 9.78 \text{ atm}$, $T_{t,1} = 7810^\circ \text{ R}$).



(b) Species with smaller mass fractions.

Figure 14.- Concluded.

the tests. The solid lines are for chemical nonequilibrium with other modes in equilibrium, while the dashed lines represent complete thermodynamic equilibrium. Both sets of data were taken from the computer program described in Reference 12. The vertical dashed line indicates the area ratio where vibration is predicted to freeze according to the criterion to be described below. Note that all species except N, NO⁺, and E⁻ are frozen at this point. The nonfrozen species are present only in very small quantities.

The criterion used to establish the vibrational freezing point was that of Phinney (Refs. 53 and 54). The freezing point is defined as the location where

$$\frac{dE}{dt} = \frac{E}{\tau_v} \quad (25)$$

E is the equilibrium vibrational energy of the gas, and τ is the vibrational relaxation rate. This criterion is similar to that for recombination freezing given in Reference 55. dE/dt was approximated as

$$\frac{\Delta E}{\Delta t} = \left| \frac{E_3 - E_1}{t_3 - t_1} \right| = \left| \frac{(E_3 - E_1) \left(\frac{u_3 + u_1}{2} \right)}{x_3 - x_1} \right| \quad (26)$$

where E and τ_v were calculated at point 2, 1 was upstream, and 3 downstream of 2 (the point in question).

The relaxation rate used was that for N₂ in air. This rate was determined by using measurements of τ_{v,N_2} obtained during the present studies and fitting various rate equations of the form

$$\tau_P = A_1 \exp\left(\frac{A_2}{T^{1/3}}\right) \quad (27)$$

where $T = ^\circ K$, $P = \text{atm}$, to the experimental data by use of the N_2 vibrational nonequilibrium program of Erickson (Ref. 56). The vibrational temperature data will be discussed under results and discussion.

The vibrational modes of the diatomic molecules N_2 , O_2 , NO , and NO^+ do not necessarily relax at the same rate. However, due to uncertainties in the relaxation rates of the other diatomic species, as well as the fact that N_2 forms the bulk of the diatomic molecules present, the use of the N_2 vibrational rate for the gas seems justified.

Once the freezing criterion set forth above was satisfied, the chemical nonequilibrium program was terminated and all fluid properties were tabulated at that station. From this point on, the chemical composition and the vibrational energy were considered frozen.

This assumption of frozen flow allows the use of perfect gas relations with an effective ratio of specific heats to calculate the flow properties downstream of the freezing point. This effective ratio of specific heats is dependent on the composition at the freezing point and may be defined as

$$\gamma_{\text{eff}} = \frac{C_{P\text{eff}}}{C_{V\text{eff}}} = \frac{\frac{7}{5} R'_M + R'_A}{R'_M + \frac{3}{5} R'_A} \quad (28)$$

where

$$R'_M = R_u [\eta'_{N_2} + \eta'_{O_2} + \eta'_{NO} + \eta'_{NO^+}] \quad (29)$$

and

$$R'_A = R_u [\eta'_{E^+} + \eta'_N + \eta'_O + \eta'_{Ar}] \quad (30)$$

The reference properties used in the frozen expansion are those at the freezing station. Properties at this station are denoted by a superscript ('). The perfect gas property relationships may be found in several references (e.g., Refs. 8 and 57).

The properties at different points downstream of the freezing point are calculated by choosing a temperature T and calculating the other properties which are needed for comparison with the experimental measurements. Thus, in terms of T and the superscript (') freezing point properties, expressions for P , ρ , V , A/A^* , and M are as follows:

$$\frac{P}{P'} = \left(\frac{T}{T'} \right)^{\gamma_{\text{eff}}/\gamma_{\text{eff}}-1} \quad (31)$$

$$\frac{\rho}{\rho'} = \left(\frac{T}{T'} \right)^{1/\gamma_{\text{eff}}-1} \quad (32)$$

$$V = \sqrt{(V')^2 + 2C_{p_{\text{eff}}}(T' - T)} \quad (33)$$

$$\frac{A}{A^*} = \left(\frac{A'}{A^*} \right) \left[\left(\frac{T'}{T} \right)^{1/\gamma_{\text{eff}}-1} \right] \left(\frac{V'}{V} \right) \quad (34)$$

$$M = \frac{V}{\sqrt{\gamma_{\text{eff}}(R_A' + R_M')T}} \quad (35)$$

For all of the present tests, the shock layer around the pitot probe was chemically frozen since the Damköhler number for dissociation (Eq. (20)) was less than 3×10^{-2} . Vibration was also frozen according to the Damköhler number for vibration (Eq. (21)). Thus, chemistry and

vibration were assumed constant at free-stream values in the shock layer and the same effective ratio of specific heats was used behind the shock as in the free stream. So, the flow across the normal shock was a perfect gas flow with an effective ratio of specific heats, γ_{eff} , Equation (28). Expressions for the properties behind the shock and at the stagnation point may be found in Reference 57.

Frozen flow.- In frozen flow, as considered here, chemical reaction and vibrational relaxation times are infinite. Consequently, for chemically and vibrationally frozen flow, the composition of the flow as well as the chemical and vibrational energy remain constant and do not contribute to the expansion. Again, the flow expansion may be calculated as that of a perfect gas with an effective ratio of specific heats.

In the present studies, the limiting case of frozen flow was taken to be that with chemistry and vibration frozen at the values in the plenum chamber. This case along with the equilibrium limiting case indicates the bounds of any possible flow property variation.

Once again, normal shock properties were calculated by perfect gas formulae using an effective ratio of specific heats since the flow was frozen behind the shock. No equations for the normal shock properties or the free-stream properties will be given since they are all found in Reference 57.

CHAPTER V

RESULTS AND DISCUSSION

The experimental and theoretical data of these studies are presented in both dimensional and dimensionless form with the exception of the calorimeter data, the stagnation point heat-transfer data, and the axial pitot pressure distributions. Stagnation chamber properties are used to nondimensionalize the test stream properties. Total enthalpy is nondimensionalized by $R_s T_0$, while free-stream velocity is nondimensionalized by the limiting velocity for complete conversion of thermal energy to kinetic energy. The "(a)" part of a figure will always be the dimensional data, while the "(b)" part will be the dimensionless data.

Calorimeter Data

A knowledge of the total enthalpy is essential in a study of this type where one is attempting to determine the degree of nonequilibrium of the flow. A theoretical technique such as the sonic-throat method must be experimentally verified, since this method is dependent on the state of the gas as well as the throat discharge coefficient. In addition, the geometry of the heater affects the prediction of this method in swirling flows. Proof of this has been obtained by the author by simulating such swirling flows with room-temperature air (to be published).

The enthalpy measured by the total calorimeter is compared to the equilibrium sonic-throat method in Figure 15. These data were taken with two different outer electrodes as noted. Total calorimeter enthalpy ranges from 1,180 Btu/lbm to 4,020 Btu/lbm.

The comparison of $H_{t, \text{sonic throat}}$ and $H_{t, \text{CAL}}$ closely parallels the line of perfect agreement to values of $H_{t, \text{CAL}} \cong 2,500$ Btu/lbm. At higher enthalpies, the sonic-throat method increasingly overpredicts the enthalpy. This may be caused by increasing swirl in the flow due to rotation of the arc as enthalpy increases (arc speed remained constant for each electrode). The evidence of swirl or vortex flow was collected by measuring the pressure on the center of the flow (on the inner electrode) and on the wall of the contamination trap (4 inches downstream from the tip of the inner electrode). As enthalpy increased, the wall pressure grew increasingly larger than the centerline pressure (see Fig. 16). Since wall pressure was used in the sonic-throat technique, such a trend would give the results shown in Figure 15.

The reason for the increasing swirl is not definitely known, but it could be due to the effects of increasing flow contamination with increasing enthalpy. Such a trend has been measured in other facilities (Ref. 58). Attempts were made to measure the amount of contamination as a function of enthalpy during the present studies. Scatter of these data was severe, although the trend was one of increasing amounts of contamination as total enthalpy increased.

Disagreement of the sonic-throat prediction with the calorimeter at the lower enthalpy levels where swirl did not seem to be a factor

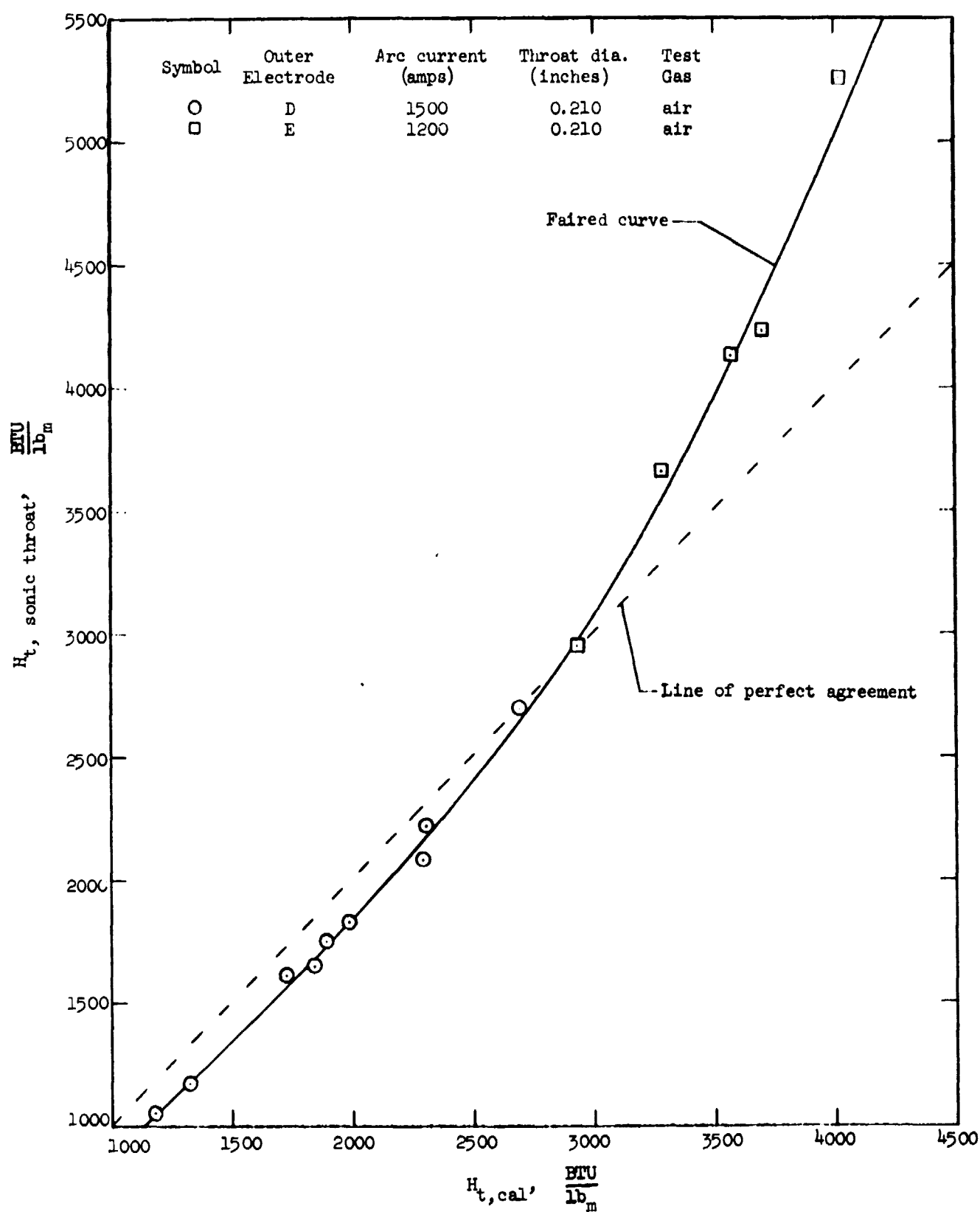


Figure 15.- A comparison of total enthalpy as calculated by the equilibrium sonic throat method with that determined from a total calorimeter.

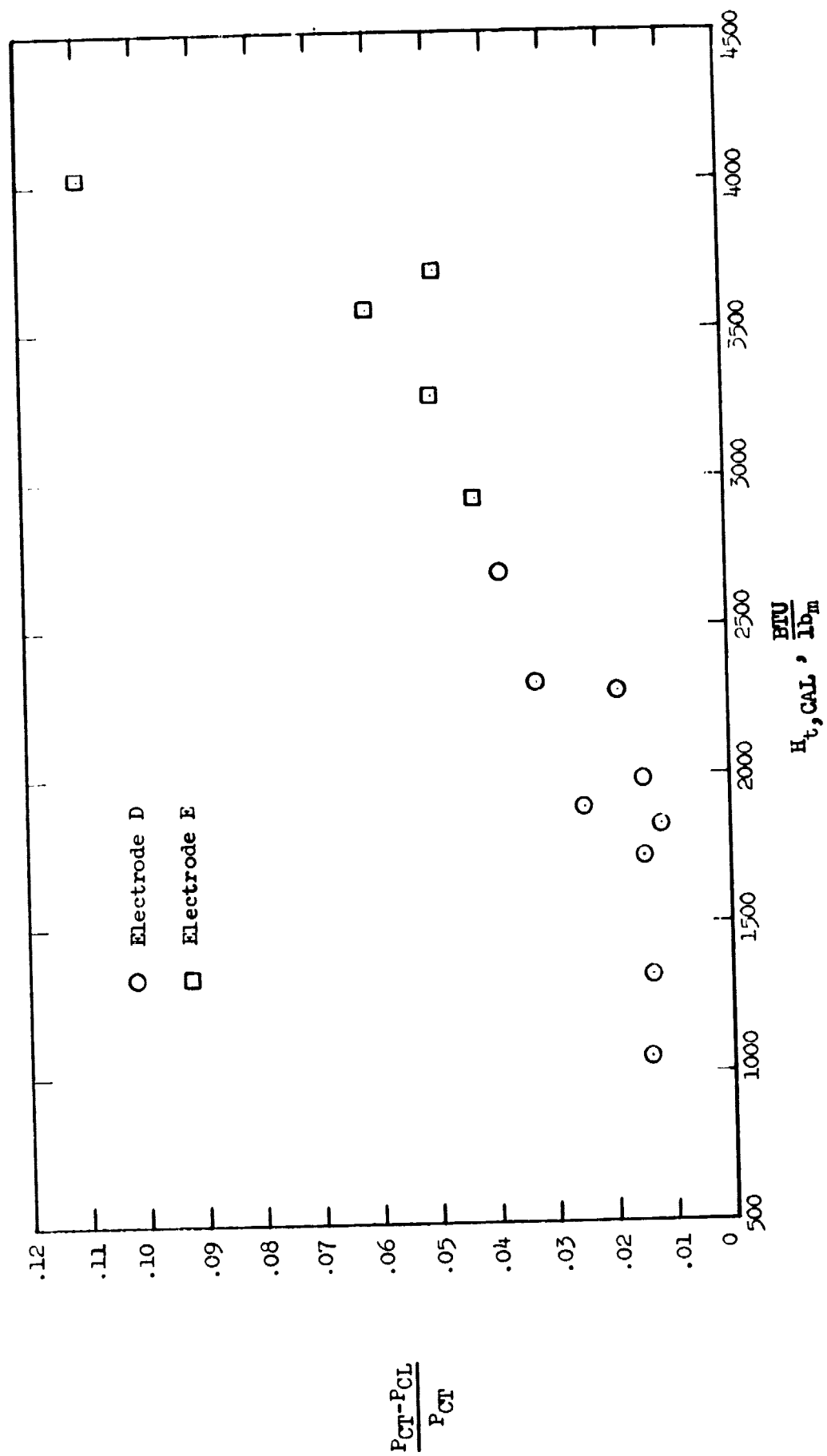


Figure 16.- Variation of the difference between arc chamber centerline and outside wall pressure with total enthalpy.

could be due either to nonequilibrium effects or to effects of arc radiation on heat losses to the throat. Experimental data obtained from the calorimeter tests are tabulated in Table II of the Appendix.

Stagnation Point Heat Transfer

Stagnation point heat-transfer rate is quite often used to predict total enthalpy in the test section of wind tunnels. However, as mentioned previously, this method is rather uncertain in low-density flows where chemistry and degree of catalycity of the gauge surface must be considered. This situation existed in the present studies as well as some uncertainty of the effective radius of the hemispherical nose section.

The stagnation point heat-transfer data are shown in Figure 17. The data are plotted as $\dot{q}/\sqrt{P_{t,2}}$; that is, no nose radius has been introduced into the experimental values. Zoby's theory for a completely catalytic wall with no consideration of second-order effects is shown for the limits of the effective nose radius. The calculations of the Damköhler number for recombination in the boundary layer indicated that the boundary layer was frozen ($C_1^* < 10^{-1}$). Thus, the uncertainty of the speed of reaction at the gauge surface must be considered in comparing the heat-transfer data with theory. This uncertainty was heightened in the present tests by deposits of contaminants on the surface. At the highest enthalpy of these tests, a spread of 30 per cent would theoretically exist between a completely

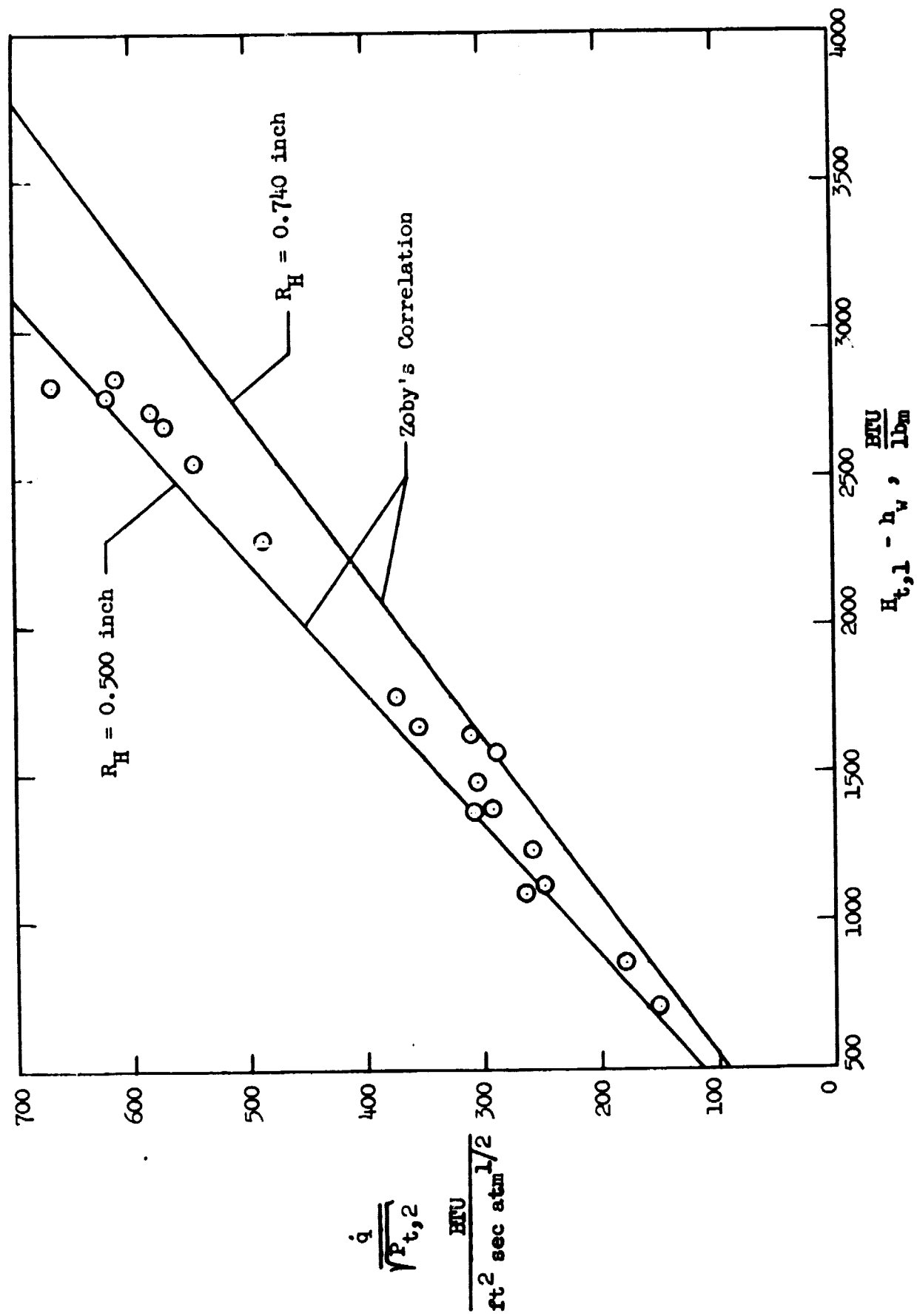


Figure 17.- A comparison of measured stagnation point heat-transfer rate with theory.

catalytic and a completely noncatalytic surface (by Eq. (14)). The present data should fall within these limits, and they do.

Previous analyses of contamination deposits in tests of this type indicated oxides of copper plated on the surface. Therefore, values of K_w were calculated for cupric oxide, using the information on surface recombination coefficients tabulated in Reference 43. At the highest value of enthalpy of the present tests, the value of heat-transfer rate for a surface covered with cupric oxide lies almost exactly between the values for a perfectly catalytic and a perfectly noncatalytic surface, or 15 per cent higher than the perfectly noncatalytic surface. This percentage decreases with decreasing enthalpy until essentially no difference is indicated between a catalytic and a noncatalytic surface at an enthalpy of approximately 1,500 Btu/lbm.

According to the theory of Cheng (Ref. 50), all of the present data are approximately 12 per cent above the high Reynolds number boundary-layer prediction because of the second-order viscous effect. The scatter of the experimental data that have been compared with this theory makes the actual magnitude of the correction somewhat questionable.

A more direct comparison with the catalytic, high Reynolds number heating-rate theory could be made if the data were corrected for chemical and second-order viscous effects. This would involve correcting the experimental data shown in Figure 17 by approximately -12 per cent to account for the viscous effect. No correction for chemistry and wall catalytic effects would be necessary below

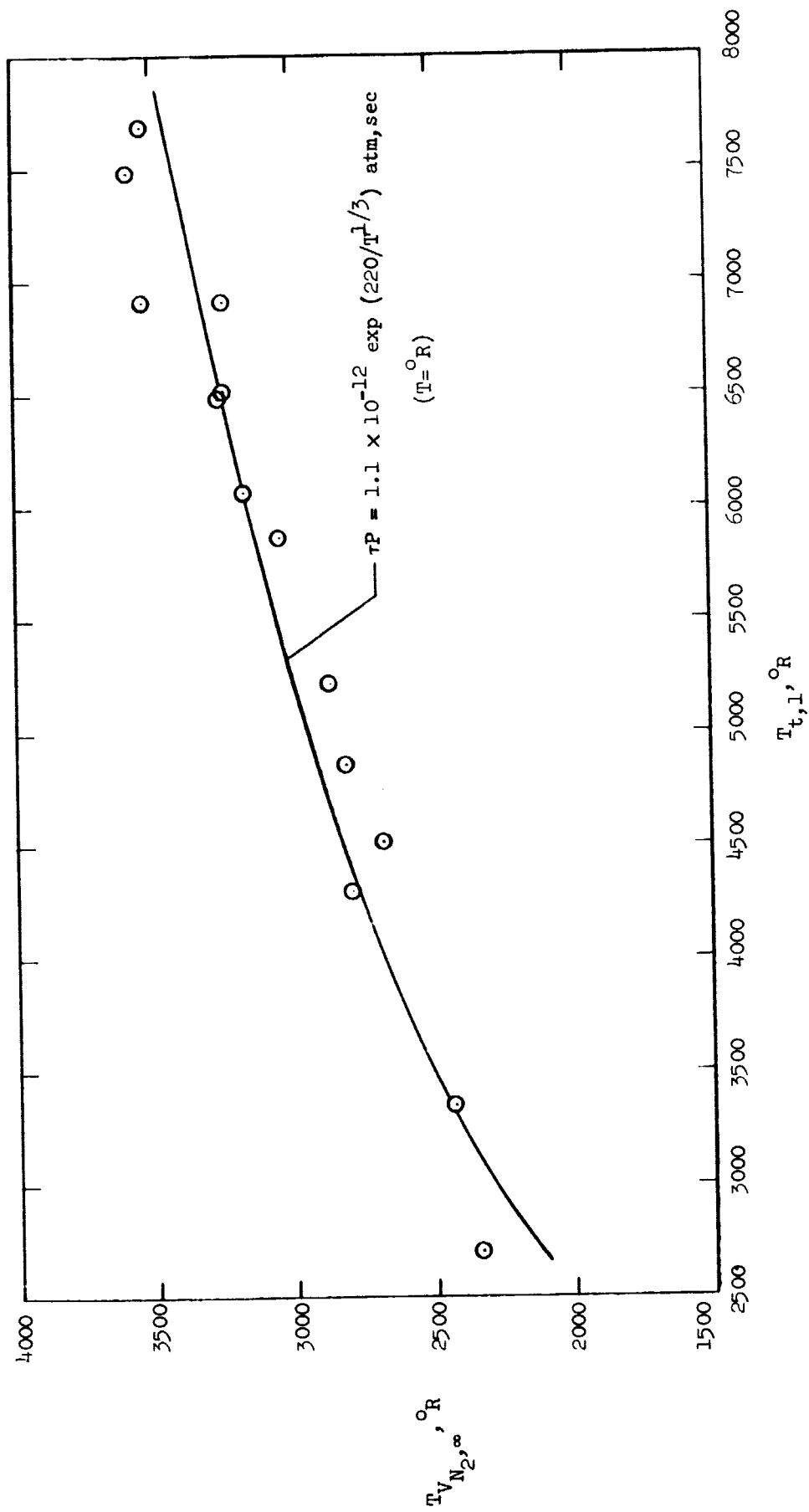
approximately 1,500 Btu/lbm. Above this level, the data should be corrected by an increasing percentage for surface catalytic effects (+15 per cent at the highest enthalpy). This is assuming that the surface is plated with cupric oxide. Thus, the data would show a net change ranging from a 12 per cent decrease at the lowest enthalpy to a 3 per cent increase at the highest enthalpy. These proposed corrections are only noted and are not applied to the data.

As can be seen from Figure 17, the limits of uncertainty on the nose radius of the heat-transfer probe impose about a 20 per cent spread on total enthalpy at a given value of heat-transfer rate. Since the data (either corrected or uncorrected for chemical and second-order viscous effects) fall between these limits, the value of total enthalpy in the free stream is certainly confirmed much closer than this (probably within ± 15 per cent).

These tests emphasize the problems associated with accurately measuring heat-transfer data in low-density, high-enthalpy facilities. Also, the critical importance of knowing the exact nose shape is obvious. Experimental data obtained from the stagnation point heat-transfer tests are tabulated in Table III of the Appendix.

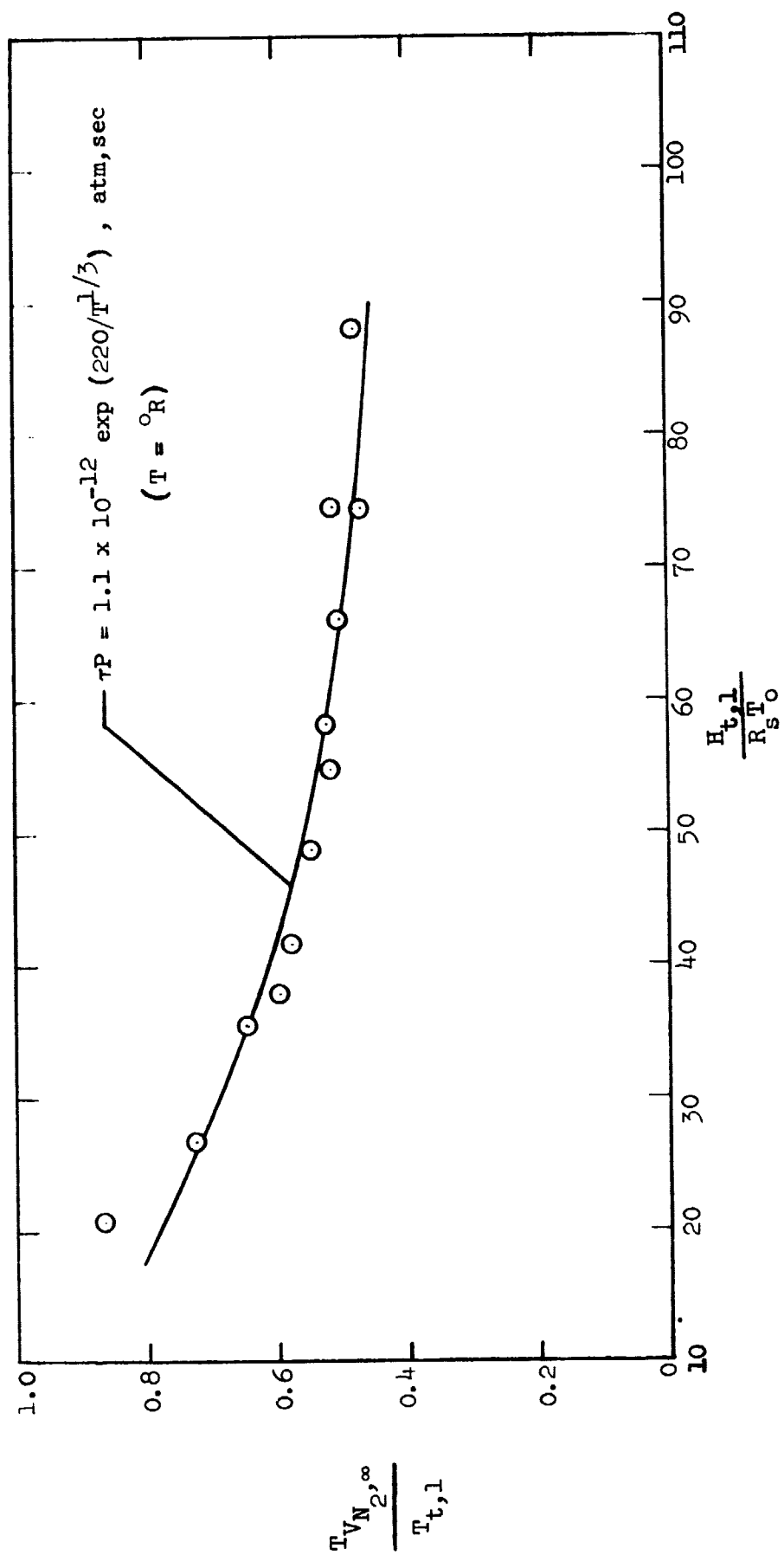
Vibrational Temperature

The vibrational temperatures were determined by comparing the relative intensities of the (0,1) and (1,2) vibrational bands of N_2^+ . The vibrational temperatures of N_2 measured in air are shown in Figure 18(a) as a function of $T_{t,1}$ and in Figure 18(b) as a function



(a) Dimensional data.

Figure 18.- Measurements of N₂ vibrational temperature illustrating the nonequilibrium nozzle flow.



(b) Dimensionless data.

Figure 18.- Concluded.

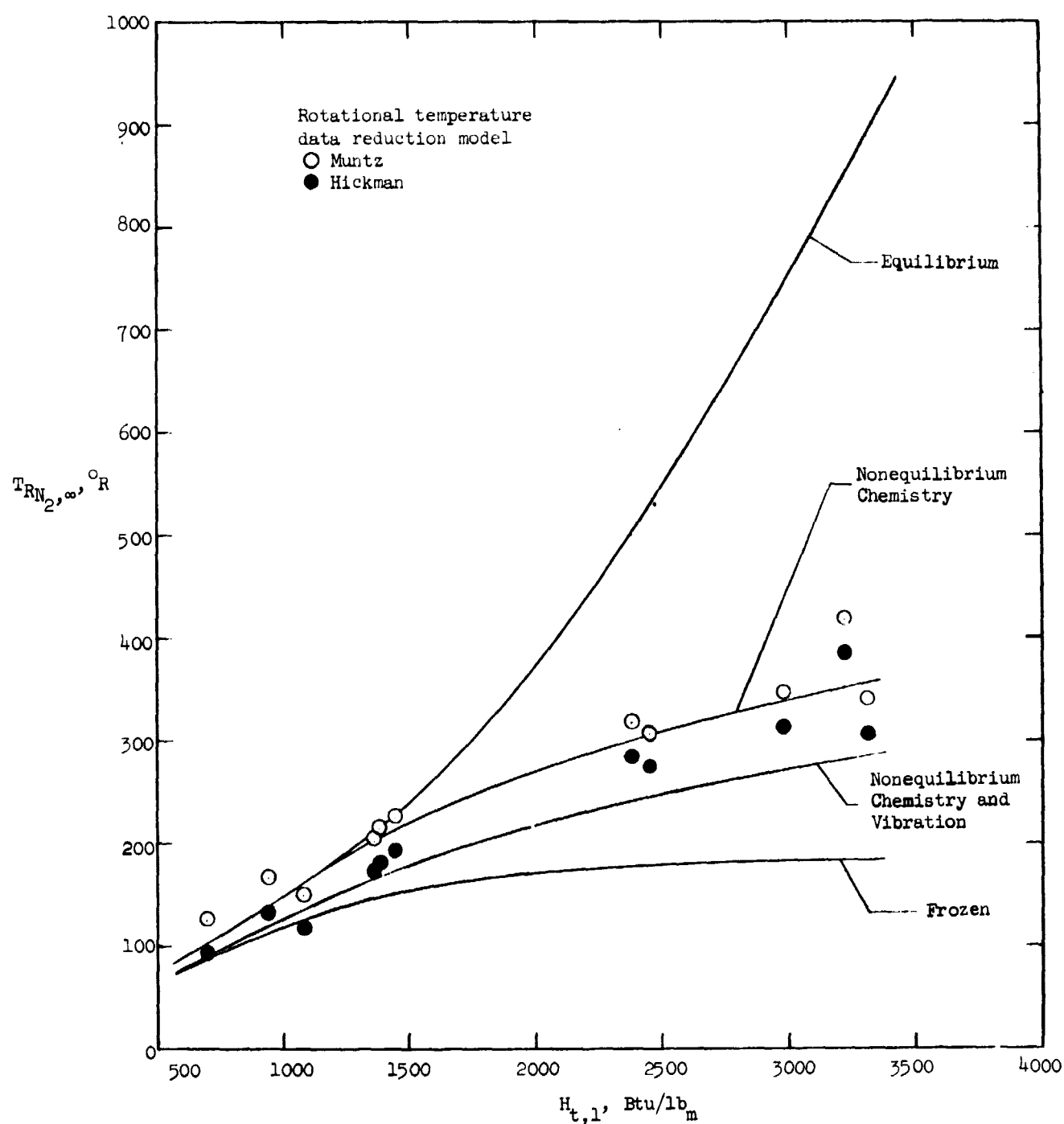
of $H_{t,1}/R_s T_0$. The fact that the vibrational temperature is not in equilibrium is shown, and these data are used to establish a rate equation for the vibrational relaxation of N_2 in air as discussed in the section on nonequilibrium flow theory. This equation was used to determine the effect of vibrational freezing on the other gas dynamic parameters of the flow. The rate equation that best fit the experimental data was

$$\tau_{VP} = 1.1 \times 10^{-12} \exp\left[\frac{181}{(T)^{1/3}}\right] \text{ atm, sec} \quad (36)$$

with T in $^{\circ}\text{K}$. These results on the N_2 vibrational relaxation rate are in agreement with the experimental results of References 7 and 18 that the relaxation rate is faster in an expanding flow than behind a normal shock (Ref. 48). The vibrational temperature data obtained from these tests are tabulated in Table IV of the Appendix.

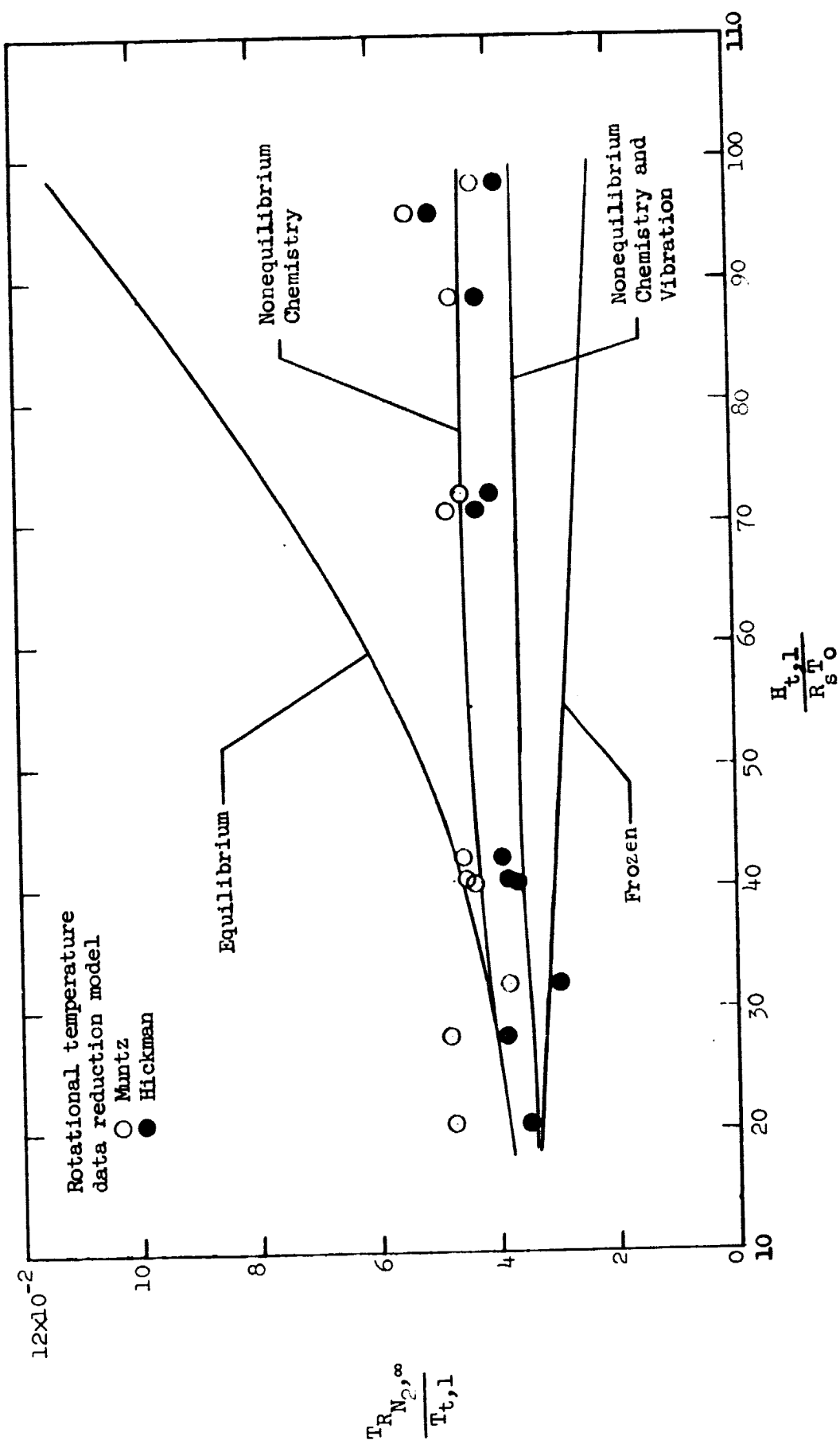
Rotational Temperature

The experimental values of rotational temperature are compared with theory in Figures 19(a) and 19(b). Although the ordinate is labeled the rotational temperature of N_2 , it is understood that rotation and translation are represented by the same kinetic temperature and that this temperature is the static temperature of the gas mixture. The curves shown are the predictions of the theories of complete thermodynamic equilibrium, chemical nonequilibrium with vibration in equilibrium, uncoupled chemical and approximate vibrational nonequilibrium, and frozen chemistry and vibration.



(a) Dimensional data.

Figure 19.- A comparison of measured N_2 rotational temperature with theoretical predictions of the nozzle expansions of gas models ranging from frozen to equilibrium.



(b) Dimensionless data.

Figure 19.- Concluded.

Two sets of symbols are shown on the figure. The open symbols are the rotational data temperature obtained using the Muntz model (Ref. 24) and the solid symbols are the data reduced according to the model proposed by Hickman (Ref. 29). Temperatures obtained using the Hickman model are in better agreement with the chemical and vibrational nonequilibrium theory, although the Muntz model is more accepted and has received wider usage. As noted earlier, the Muntz model overestimates the temperature, especially at low temperatures, although it becomes increasingly accurate as temperature increases. The per cent difference between the two models is 20 per cent at 100° R and 5 per cent at 400° R.

The Hickman model is considered to be the more accurate of the two models in lieu of its performance at the lower temperatures and in view of the results of Ashkenas' work in this density range. Note that at the lower temperatures, the data as resolved by the Muntz model lie either above or nearly coincident with the equilibrium theory up to a total enthalpy of approximately 1,500 Btu/lbm. Consideration of only the Muntz model could lead to the conclusion that vibrational equilibrium is unimportant. However, from the present calculations and the work of Erickson (Ref. 56), the degree of vibrational nonequilibrium must clearly be taken into account. Hence, in speaking of the rotational temperature data henceforth, the reference will be to the data as reduced by Hickman's model.

Generally, the data lie slightly above the chemical and vibrational nonequilibrium theory over the entire range of total enthalpy.

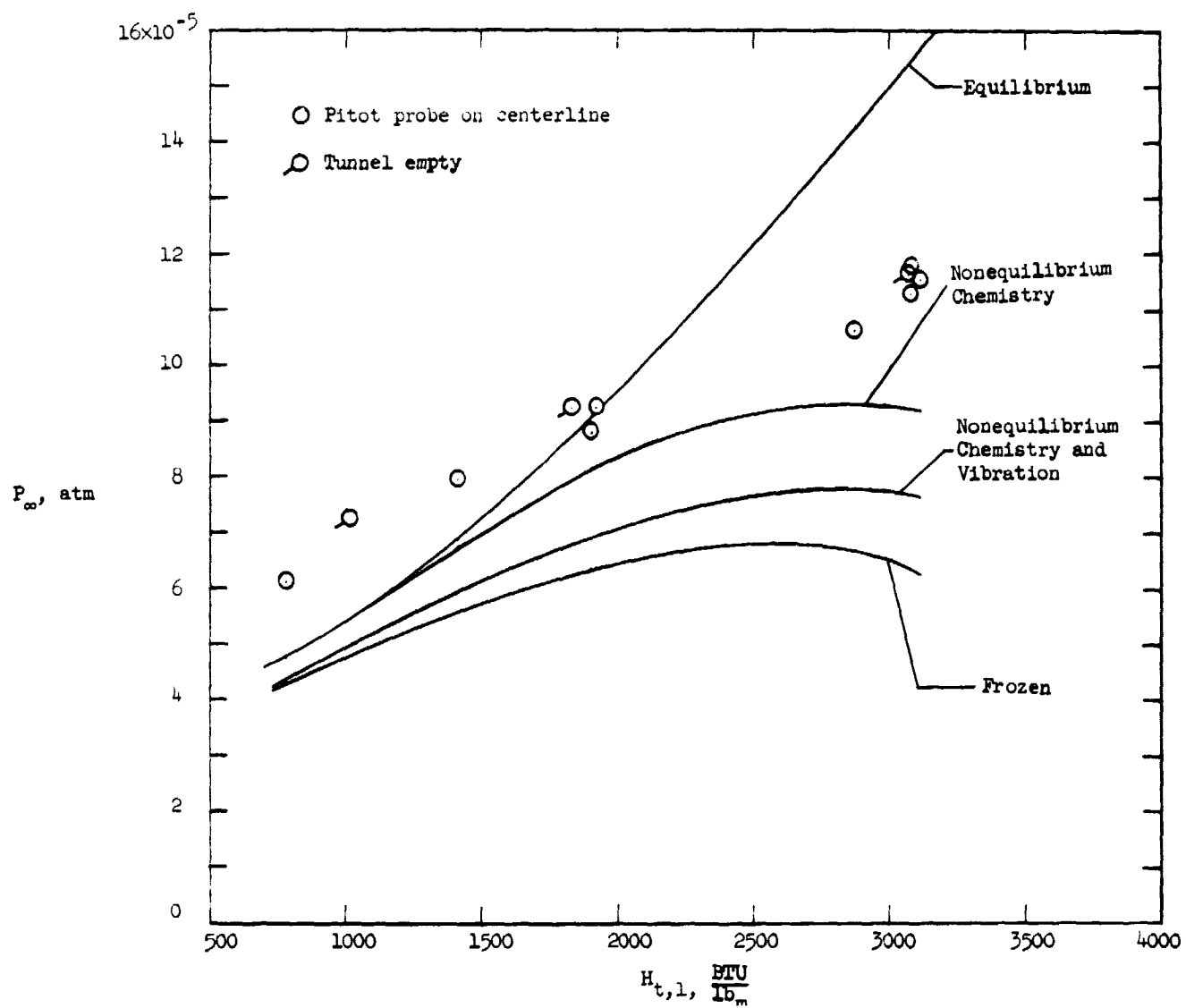
It is difficult to comment on the model used to simulate vibrational nonequilibrium, since the data lie equally close to the curve for chemical nonequilibrium with vibration in equilibrium.

One conclusion that may be drawn from this figure is that the gas is in a nonequilibrium state. The rotational temperature reduction methods are certainly sufficiently accurate to confirm that the flow is neither in equilibrium nor completely frozen. Also, within the probable accuracy of the data reduction models, the chemical and vibrational nonequilibrium theory proposed in this report is in reasonable agreement with the data. Final judgment of this theory can only be made after comparison with the other measured parameters. The rotational temperature data are tabulated in Table V of the Appendix.

Nozzle Wall Static Pressures

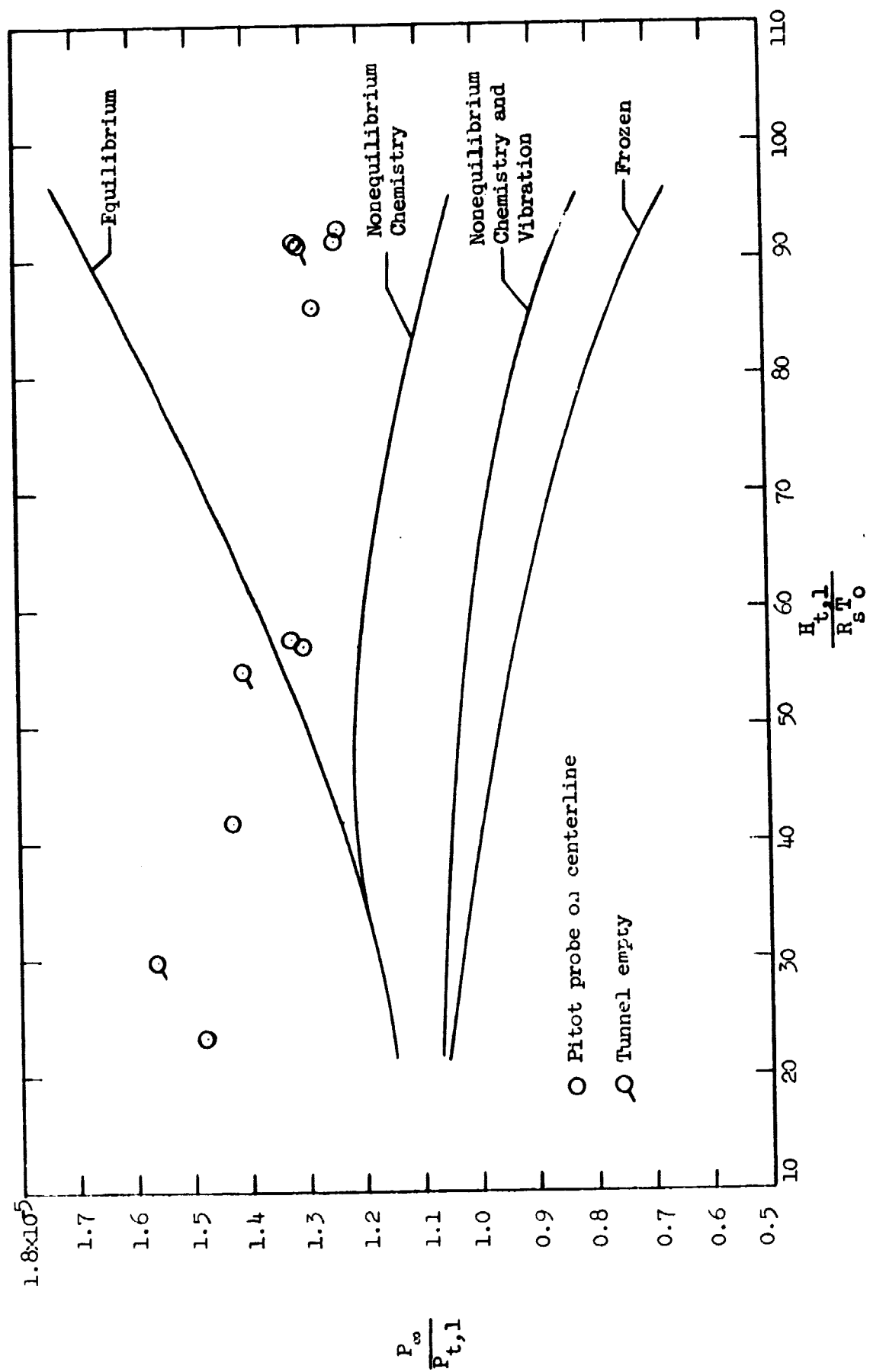
The nozzle wall static pressure data are presented in Figures 20(a) and 20(b) as a function of total enthalpy. The open symbols were obtained with the 1/4-inch-diameter flat-faced cylindrical pitot probe located on the tunnel centerline, while the flagged-open symbols were made with no probe in the tunnel. Thus, it is evident that the presence of the probe did not affect the wall static pressures.

The data have been corrected for the heat-transfer orifice effect (Refs. 33 and 34). A 3 per cent to 12 per cent upward correction with increasing enthalpy was necessary. No corrections were made



(a) Dimensional data.

Figure 20.- A comparison of measured wall static pressure with theoretical predictions of the nozzle expansions of gas models ranging from frozen to equilibrium.



(b) Dimensionless data.

Figure 20. - Concluded.

for static pressure variation across the flow core as was done in Reference 7, since no clear-cut method was available to make such a correction.

The need for some further correction to the pressure data is obvious if one considers the lower enthalpy data. Note that the spread between the frozen and equilibrium theories is approximately 15 per cent at 1,000 Btu/lbm, while the experimental data lie about 30 per cent above the equilibrium theory. The experimental measurements should be accurate to within approximately 5 per cent at this pressure level. Thus, neither the accuracy of the data nor the possible spread due to the state of the gas can account for the observed disagreement with theory.

The data lie considerably above nonequilibrium theory over the entire range of enthalpy and cross equilibrium theory at approximately 1,900 Btu/lbm. Compression waves caused by the contouring effect of the boundary layer and/or lateral flow gradients could tend to make the wall pressure higher than centerline pressure.

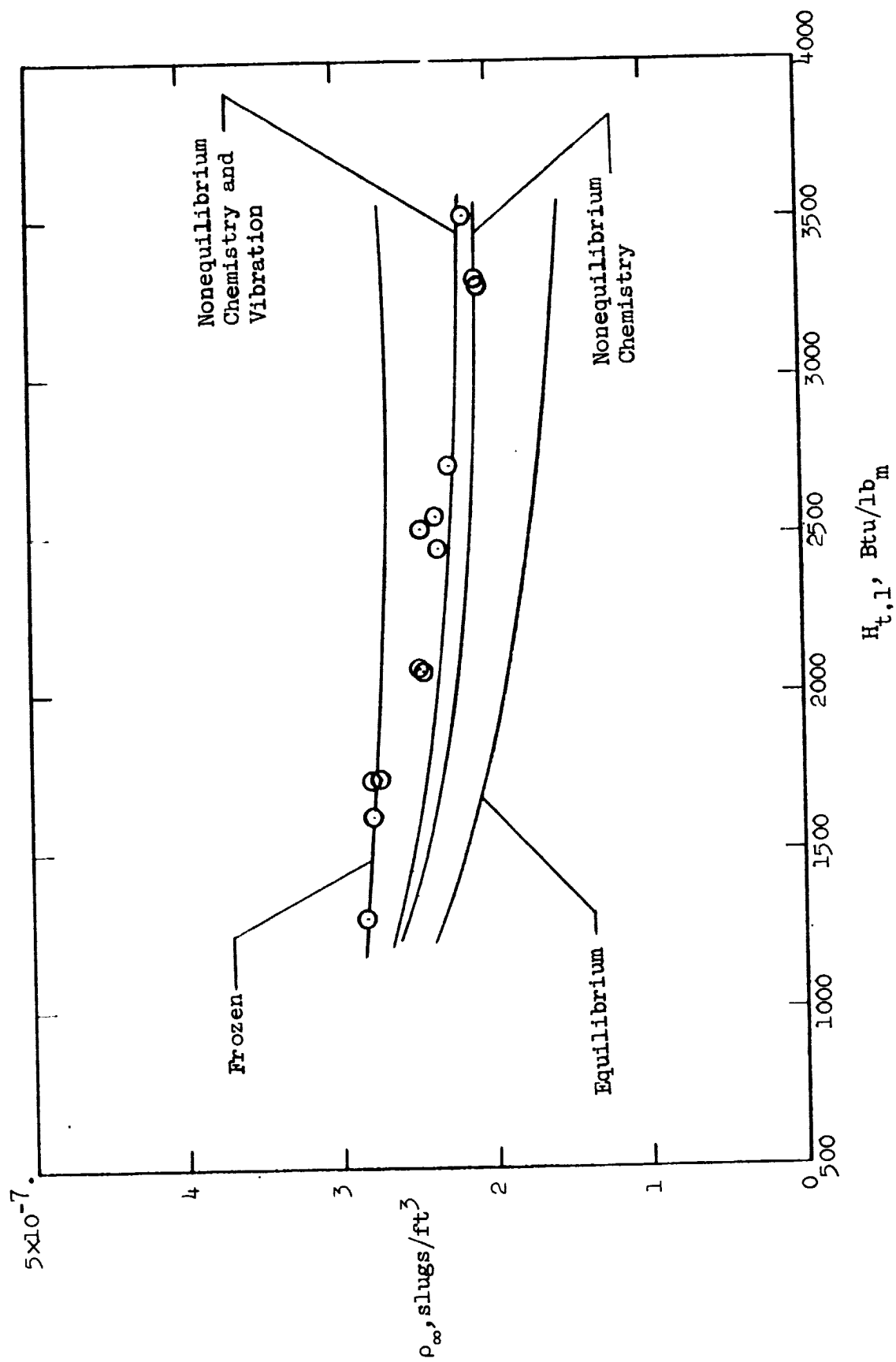
Thus, the wall static pressures are inadequate (at this high area ratio) for the determination of the proper expansion model. A "calculated" experimental centerline static pressure using the measured rotational temperature and the measured free-stream density from the mass flow probe (to be presented in the next section) could be calculated from the thermal equation of state, $P = Z\rho R_g T$, since $Z_{t,1}$ only varies from 1.00 to 1.14. However, the uncertainty involved with the

rotational temperatures negates this approach. The experimental static pressure data are tabulated in Table VI of the Appendix.

Static Density

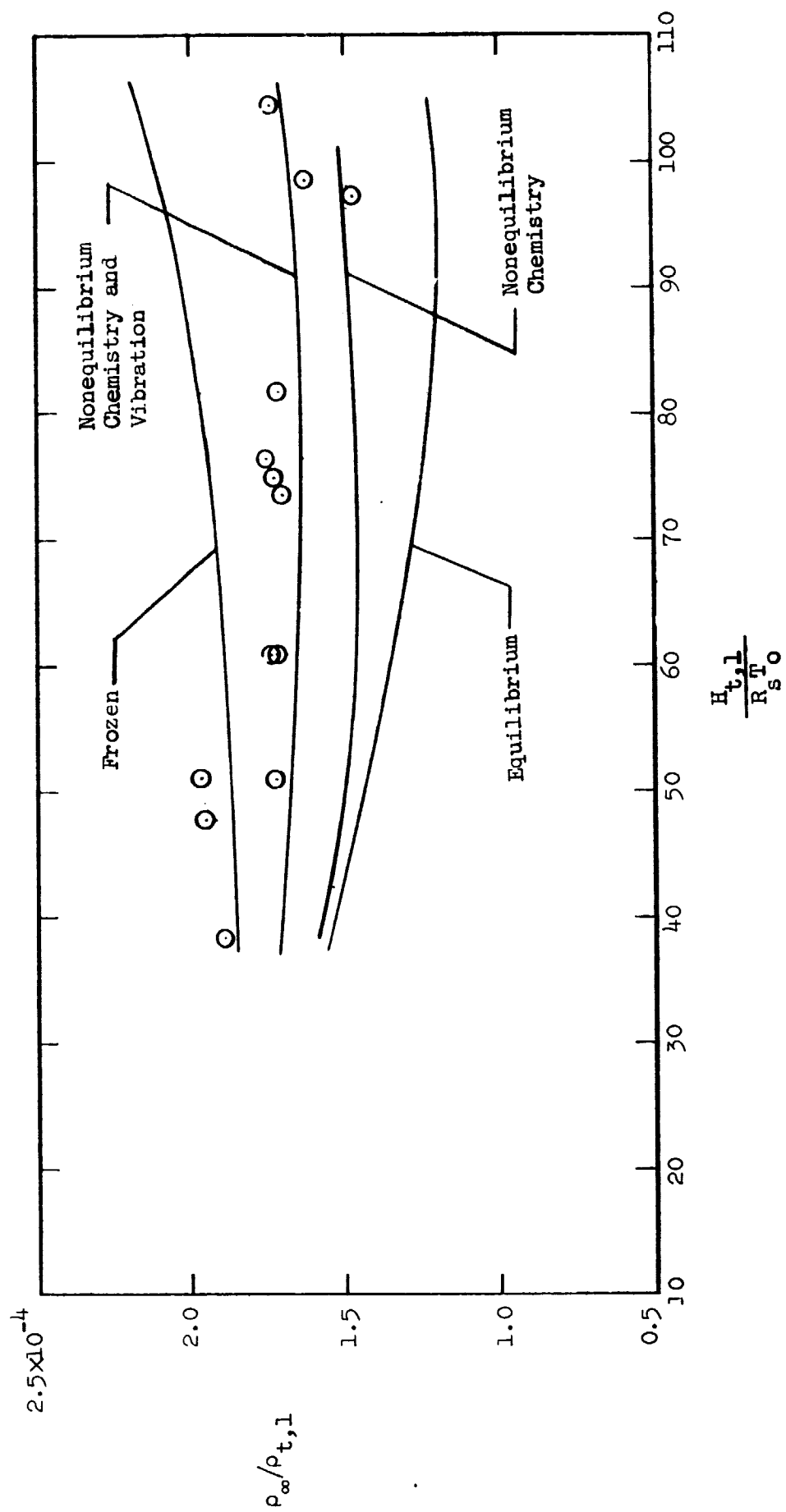
The free-stream static density, as determined from the mass flow probe, is shown as a function of total enthalpy in Figures 21(a) and 21(b). The chemical and vibrational nonequilibrium theory agrees well with the experimental values of density above approximately 2,000 Btu/lbm. Below 2,000 Btu/lbm, the data gradually trend upward to the frozen expansion theory. The spread between nonequilibrium and frozen theory is on the order of 10 per cent in this enthalpy range, however, and this upward trend could be simply data scatter. Another possibility for the discrepancy is the factor B used in the relationship between pitot pressure and the product of free-stream velocity and pressure, that is, $P_{t,2} = B\rho_{\infty}V_{\infty}^2$. In these tests, B was assumed to be constant at 0.925, although it is weakly dependent on the effective value of the ratio of specific heats.

The density data generally confirm the nonequilibrium theory proposed in this report. Although the lower enthalpy data are difficult to interpret, the spread between frozen and equilibrium flow at the higher enthalpies and the good agreement of the experimental data with the chemical and vibrational nonequilibrium theory in this range enable one to arrive at the preceding conclusion. The experimental density data are tabulated in Table VII of the Appendix.



(a) Dimensional data.

Figure 21.- A comparison of measured static density with theoretical predictions of the nozzle expansions of gas models ranging from frozen to equilibrium.



(b) Dimensionless data.

Figure 21.- Concluded.

Velocity

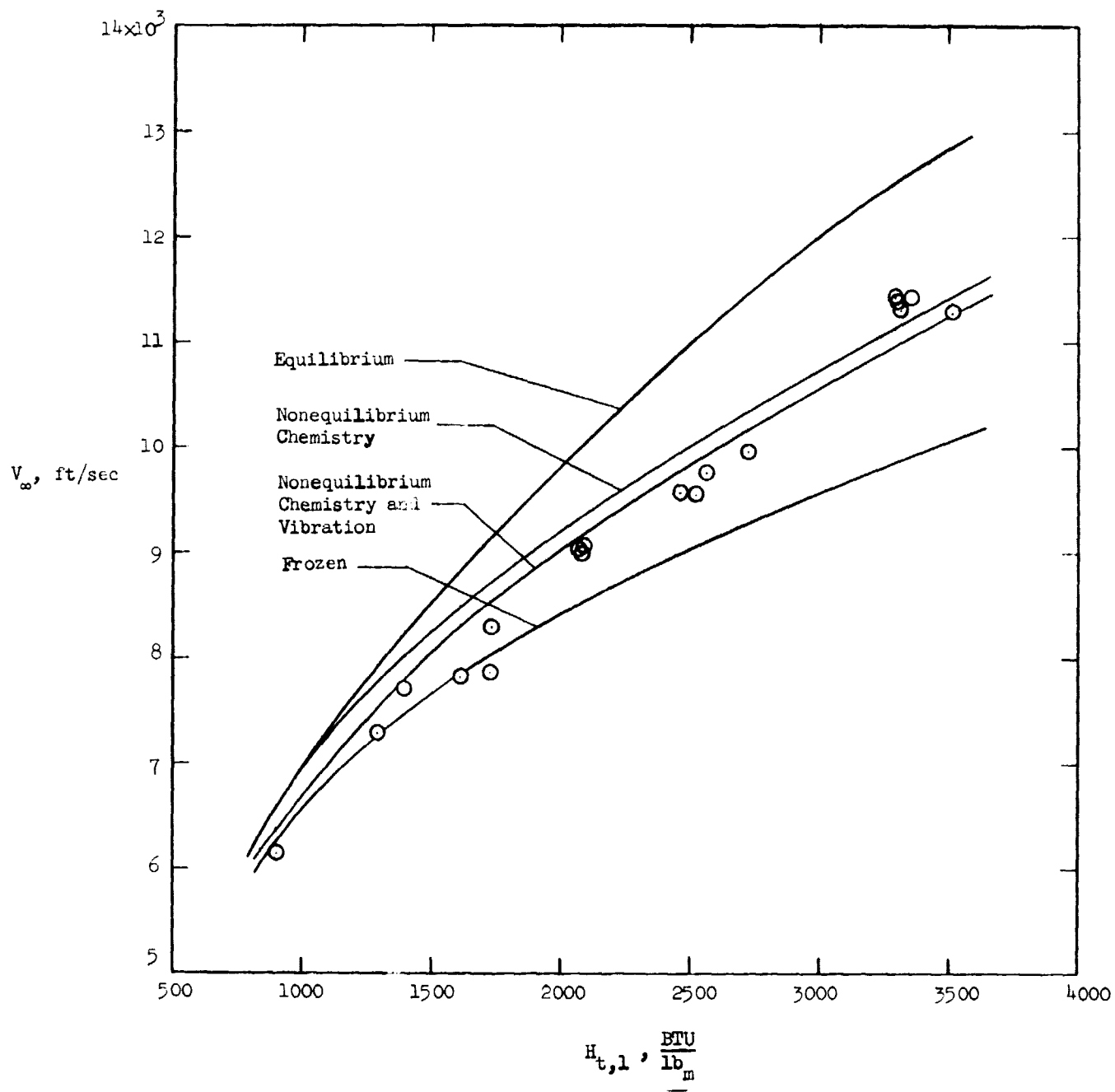
The velocity measurements obtained from the mass flow probe are shown in Figures 22(a) and 22(b) as a function of total enthalpy. The chemical and vibrational nonequilibrium theory generally is in much closer agreement with the experimental data than are the other theoretical gas models. At the lower enthalpies, as in the case of density, the velocity data fall onto the frozen theory prediction. The possible source of this behavior has been discussed previously in the section concerning free-stream density.

The good agreement with nonequilibrium theory serves to give one confidence in the present theoretical formulation. The allowance for vibrational freezing is reasonably verified when one compares the chemical nonequilibrium theory (vibration in equilibrium) with the experimental data. The experimental velocity data are tabulated in Table VII of the Appendix.

Pitot Pressure Gradients

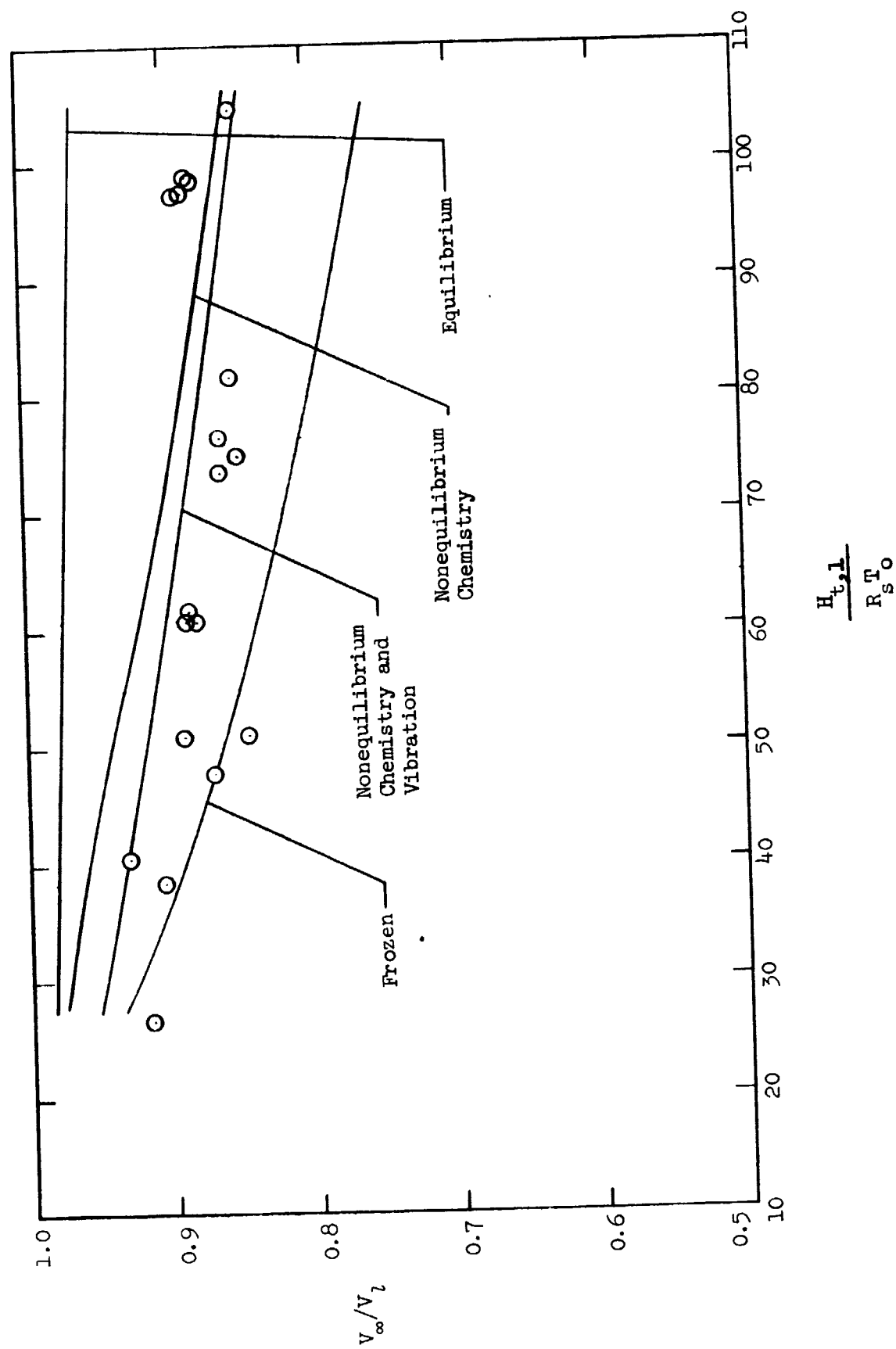
All of the pitot pressure data accumulated during the present experiments are shown in Figure 23 as a function of total enthalpy. These data were obtained with the various probes noted on the figure at locations of -6, 2-1/4, and 13 inches from the nozzle-test section juncture.

The composite of these data is effectively an axial survey of the pitot pressure on the centerline of the tunnel. With a knowledge of the proper gas expansion model, one can specify flow gradients, such



(a) Dimensional data.

Figure 22.- A comparison of measured free-stream velocity with theoretical predictions of the nozzle expansions of gas models ranging from frozen to equilibrium.



(b) Dimensionless data.

Figure 22.- Concluded.

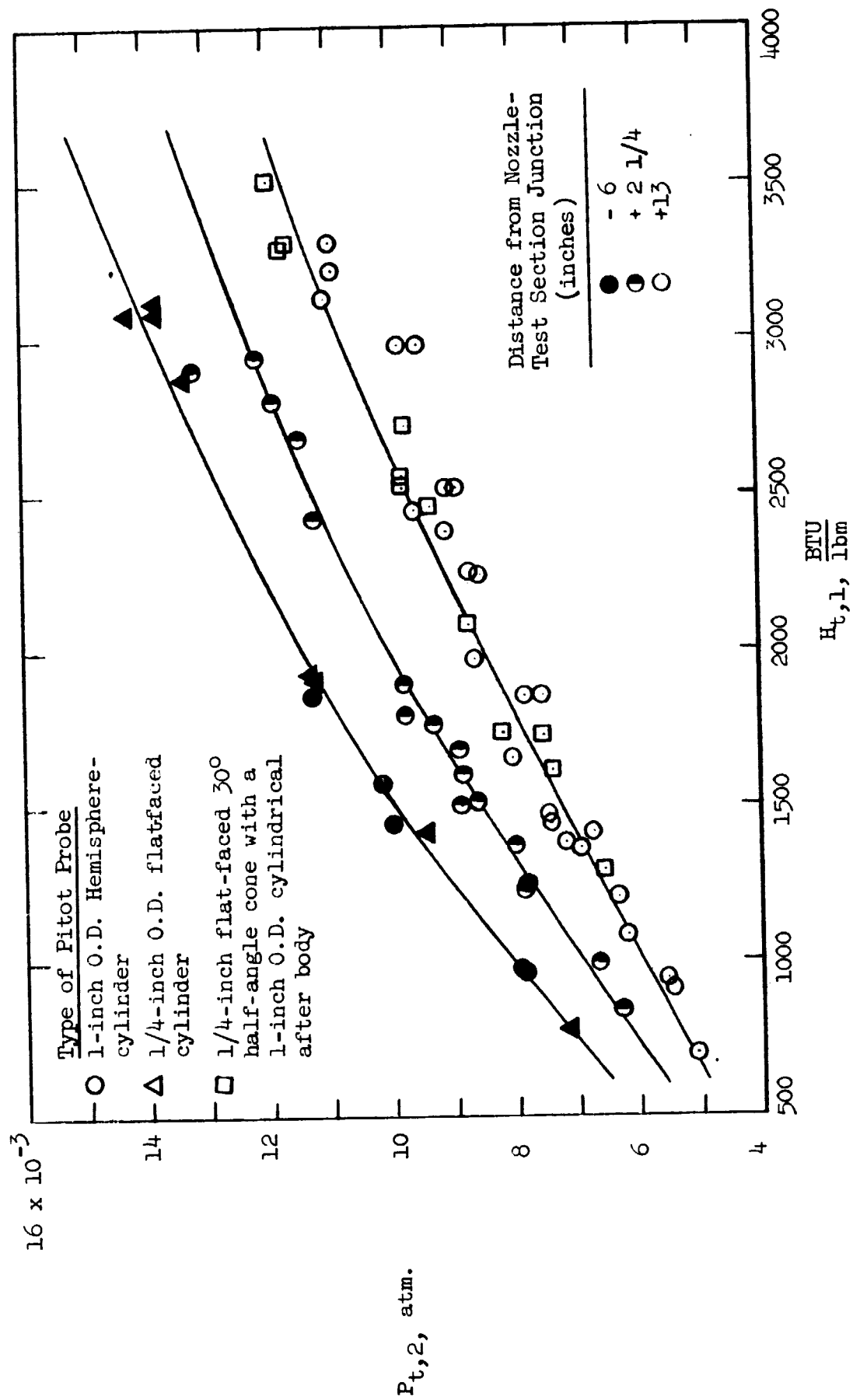


Figure 23.- Axial pitot pressure distribution as a function of total enthalpy.

as the longitudinal Mach number gradient. The Mach number gradient is approximately 0.06 per inch at 700 Btu/lbm and approximately 0.035 per inch at 3,500 Btu/lbm.

CHAPTER VI

CONCLUDING REMARKS

A series of tests have been performed to calibrate and diagnose the flow in an electric arc heated test stream of air. Tests were made over a range of plenum chamber conditions with plenum chamber enthalpy varying from 700 to 3,510 Btu/lbm and plenum chamber pressure varying from 4.20 to 9.38 atmospheres. Parameters measured during the tests were N_2 vibrational temperature, N_2 rotational temperature, wall static pressure, static density, velocity, total enthalpy, and hemisphere stagnation point heat-transfer rate.

Based on the results of these tests, the following conclusions can be made:

(1) The rotational temperature data indicate that the flow is in a nonequilibrium state since the data fall between the prediction of the chemical nonequilibrium theory with and without vibrational nonequilibrium. Results from Hickman's data reduction technique for obtaining the rotational temperature were in closer agreement with the chemical nonequilibrium sudden-vibrational freezing theory than were the results of Muntz's method. The percent difference between the two methods ranged from 20 percent at $100^\circ R$ to 5 percent at $400^\circ R$.

(2) Measured density and velocity (obtained from the mass flow probe) generally agreed with the predictions of the chemical nonequilibrium, sudden-vibrational freezing theory. The consistency of the

experimental data and the good agreement of these data with theory support the design of the mass flow probe with equal interior and exterior tip angles.

(3) Measurements of N_2 vibrational temperature in air indicated vibrational freezing just downstream of the nozzle throat. The data were used to obtain a vibrational relaxation rate equation. The vibrational temperature data also supported the results of other investigators that the vibrational mode relaxes faster during an expansion than behind a normal shock.

(4) Wall static pressures were inconclusive in establishing the proper gas flow model to use for the nozzle expansion. Weak compression waves caused by boundary layer countouring may be the cause of the high measured pressure data. However, the static pressure data definitely confirm that the flow is in a nonequilibrium state.

(5) The sonic-throat technique for predicting stagnation enthalpy should be experimentally verified before relying upon the method. This is evident from the present tests where such factors as swirl, heater geometry, and the thermodynamic state of the gas cause deviation from equilibrium sonic-throat predictions.

(6) The comparison of stagnation point heat-transfer data with theory was affected by uncertainty of the surface catalytic efficiency, the magnitude of the second-order viscous effect, and the uncertainty of the hemisphere nose radius. However, the free-stream total enthalpy could still be verified to approximately ± 15 per cent by the use of the heat-transfer measurements.

Thus, the conclusions generally point to acceptable agreement of the various measured experimental data with the predictions of a chemical nonequilibrium, vibrational sudden-freeze technique for calculating the nozzle expansion of the air. Several pertinent free-stream parameters can be determined by using this flow expansion gas model. At a location 2-1/4 inches from the nozzle test section juncture, the Mach number varies from 11.2 to 12.3 over a total enthalpy range from 700 to 3,500 Btu/lbm. This corresponds to a stagnation chamber pressure range from 4.20 to 9.40 atmospheres. Reynolds number per foot at this location varies from 3×10^4 to 1×10^4 , while the Mach number axial gradient varies from 0.06 per inch to 0.035 per inch over this same range of supply conditions.

REFERENCES

1. Nagamatsu, H. T.; Workman, J. B.; and Sheer, R. E., Jr.: Hypersonic Nozzle Expansion of Air With Atom Recombination Present. *J. Aero. Sci.*, vol. 28, no. 11, Nov. 1961, pp. 833-837.
2. Duffy, Robert E.: A Static-Pressure Measurement for Chemical Kinetic Studies. First International Conference on Instrumentation in Aerospace Simulation Facilities, Paris, France, Sept. 28-29, 1964, pp. 23 (1-18).
3. Duffy, Robert E.: Experimental Study of Nonequilibrium Expanding Flows. *AIAA J.*, vol. 3, no. 2, Feb. 1965, pp. 237-244.
4. Nagamatsu, H. T.; and Sheer, R. E., Jr.: Vibrational Relaxation and Recombination of Nitrogen and Air in Hypersonic Nozzle Flows. *AIAA J.*, vol. 3, no. 8, Aug. 1965, pp. 1386-1391.
5. Petrie, S. L.; Pierce, G. A.; and Fishburne, E. S.: Analysis of the Thermo-Chemical State of an Expanded Air Plasma. USAF FDL TR-64-191, Aug. 1965.
6. Zonars, D.: Nonequilibrium Regime of Airflows in Contoured Nozzles: Theory and Experiments. *AIAA J.*, vol. 5, no. 1, Jan. 1967, pp. 57-63.
7. MacDermott, W. N.; and Marshall, J. C.: Theoretical and Experimental Nonequilibrium Expansions of Partially Dissociated Air. AIAA Fourth Aerodynamic Testing Conference, Cincinnati, Ohio, Apr. 28-30, 1969, pp. 69-328 (1-13).
8. Heims, Steve P.: Effects of Chemical Dissociation and Molecular Vibrations on Steady One-Dimensional Flow. NASA TN D-87, Aug. 1959.
9. Glowacki, W. J.: Effect of Finite Oxygen Recombination Rate on the Flow Conditions in Hypersonic Nozzles. Aeroballistic Research Report No. 148, Naval Ordnance Lab. NOL TR-61-23, U.S. Naval Ordnance Lab., White Oak, Maryland.
10. Enkenhus, K. R.: Analytical Study of Non-Equilibrium Flow in Hypersonic Nozzles Using a Simplified Model for Air. NOL TR 66-104, Jan. 1967.

11. Emanuel, George; and Vincenti, Walter G.: Method for Calculation of the One-Dimensional Nonequilibrium Flow of a General Gas Mixture Through a Hypersonic Nozzle. AEDC-TDR-62-131, June 1962.
12. Lordi, J. A.; Mates, R. E.; and Moselle, J. R.: Computer Program for the Numerical Solution of Nonequilibrium Expansions of Reacting Gas Mixtures. CAL Report No. AD-1589-A-6, Oct. 1965.
13. Tirumalesa, Duvvuri: Nozzle Flows With Coupled Vibrational and Dissociational Nonequilibrium. UTIAS Report No. 123, Aug. 1967.
14. Dressler, H. S.; French, E. P.; and Webb, H. G., Jr.: Computer Program for One-Dimensional Nonequilibrium Reacting Gas Flow Space Division, North American Aviation, Inc., Tech. Rept. AFFDL-TR-67-75, Aug. 1967.
15. Boatright, William B.; Stewart, Roger B.; and Grimaud, John E.: Description and Preliminary Calibration Tests of a Small Arc-Heated Hypersonic Wind Tunnel. NASA TN D-1377, Dec. 1962.
16. Boatright, W. B.; Sebacher, D. I.; Guy, R. W.; and Duckett, R. J.: Review of Testing Techniques and Flow Calibration Results for Hypersonic Arc Tunnels. AIAA Paper No. 68-379, AIAA Third Aerodynamic Testing Conference, San Francisco, Calif., Apr. 8-10, 1968.
17. Sebacher, D. I.; and Duckett, R. J.: A Spectroscopic Analysis of a 1-Foot Hypersonic-Arc-Tunnel Airstream Using an Electron Beam Probe. NASA TR R-214, Dec. 1964.
18. Sebacher, Daniel I.: An Electron Beam Study of Vibrational and Rotational Relaxing Flows of Nitrogen and Air. Proceedings of the 1966 Heat Transfer and Fluid Mechanics Institute, Santa Clara, Calif., June 22-24, 1966, pp. 315-334.
19. Crites, Roger C.; and Czysz, Paul: Inlet and Test Section Diagnostics Using a Miniature Mass Flow Probe in Hypersonic Impulse Tunnel. AIAA Paper No. 68-389, AIAA Third Aerodynamics Testing Conference, San Francisco, Calif., Apr. 8-10, 1968.
20. Gardon, Robert: Instrument for the Direct Measurement of Intense Thermal Radiation. Review of Scientific Instruments, vol. 24, no. 5, May 1953.
21. Winovich, Warren: On the Equilibrium Sonic-Throat Method for Evaluating Electric-Arc Air-Heater Performance. NASA TN D-2132, 1964.

22. Jorgensen, Leland H.: The Total Enthalpy of a One-Dimensional Nozzle Flow With Various Gases. NASA TN D-2233, March 1964.
23. Hoppe, John C.: Rotational and Vibrational Temperature Measurements in the 12-Inch Hypersonic Ceramic-Heated Tunnel. NASA TN D-4892, Nov. 1968.
24. Muntz, E. P.: Measurement of Rotational Temperature, Vibrational Temperature, and Molecular Concentration in Non-Radiating Flows of Low-Density Nitrogen. Rep. No. 71 (AFOSR TN 60-499), Inst. Aerophys., University of Toronto, Apr. 1961.
25. Ashkenas, Harry: Rotational Temperature Measurements in Electron-Beam Excited Nitrogen. Physics of Fluids, vol. 10, no. 12, Dec. 1967, pp. 2509-2520.
26. Robben, F.; and Talbot, L.: Some Measurements of Rotational Temperatures in a Low Density Wind Tunnel Using Electron Beam Fluorescence. University of California, Berkeley, Rept. No. AS-65-5, May 1965.
27. Marrone, Paul V.: Rotational Temperature and Density Measurements in Underexpanded Jets and Shock Waves Using an Electron Beam Probe. UTIAS Rept. No. 113, Jan. 1966.
28. Tirumalesa, Duvvuri: Rotational Relaxation in Hypersonic Low-Density Flows. AIAA J., vol. 6, no. 4, Apr. 1968, pp. 765-766.
29. Hickman, Roy Scott: Rotational Temperature Measurements in Nitrogen Using an Electron Beam. University of Southern California, USCAE 104, AFOSR 66-2509, Sept. 1966.
30. Lillicrap, D. C.; and Harvey, J. K.: Electron-Beam Rotational Temperature Measurements Including the Effect of Secondary Electrons. AIAA J., vol. 7, no. 5, May 1969, pp. 980-982.
31. Hayes, Wallace D.; and Probstein, Ronald R.: Hypersonic Flow Theory. Academic Press, 1959.
32. Arney, G. D., Jr.; and Bailey, A. B.: Addendum to an Investigation of the Equilibrium Pressure Along Unequally Heated Tubes. AEDC-TDR-62-188, Oct. 1962.
33. Potter, J. Leith; Kinslow, Max; and Boylan, David E.: An Influence of the Orifice on Measured Pressures in Rarefied Flow. AEDC-TDR-64-175, Sept. 1964.

34. Guy, R. W.; and Winebarger, R. M.: Effect of Orifice Size and Heat Transfer Rate on Measured Static Pressures in a Low-Density Arc-Heated Wind Tunnel. NASA TN D-3829, Feb. 1967.
35. Daum, F. L.; Shang, J. S.; and Elliott, G. A.: Impact Pressure Behavior in Rarefied Hypersonic Flow. AIAA J., vol. 3, no. 8, Aug. 1965, pp. 1546-1548.
36. Schaaf, S. A.: The Pitot Probe in Low-Density Flow. AGARD Report No. 525, Jan. 1966.
37. Zoby, Ernest V.: Effects of Corner Radius on Stagnation-Point Velocity Gradients on Blunt Axisymmetric Bodies. NASA TM X-1067, Mar. 1965.
38. Ellison, James C.: Experimental Stagnation-Point Velocity Gradients and Heat-Transfer Coefficients for a Family of Blunt Bodies at Mach 8 and Angles of Attack. NASA TN D-5121, Apr. 1969.
39. Stallings, Robert L.: Experimentally Determined Local Flow Properties and Drag Coefficients for a Family of Blunt Bodies at Mach Numbers From 2.49 to 4.63. NASA TR R-274, Oct. 1967.
40. Zoby, Ernest V.: Empirical Stagnation-Point Heat Transfer Relation in Several Gas Mixtures at High Enthalpy Level. NASA TN D-4799, Oct. 1968.
41. Rosner, Daniel E.: Scale Effects and Correlations in Nonequilibrium Convective Heat Transfer. AIAA J., vol. 1, no. 7, July 1963, pp. 1550-1555.
42. Fay, J. A.; and Riddell, F. R.: Theory of Stagnation Point Heat Transfer in Dissociated Air. J. Aeros. Sci., vol. 25, no. 2, Feb. 1958, pp. 73-85.
43. Hartunian, R. A.; and Marrone, P. V.: Heat Transfer From Dissociated Gases in a Shock Tube. CAL Report No. AD-1118-A-7 (AFOSR TN 59-1087), Nov. 1959.
44. Carden, William H.: Experimental Heat Transfer to Hemispheres in Nonequilibrium Dissociated Hypersonic Flow With Surface Catalysis and Second-Order Effects. AEDC-TR-65-127, July 1965.
45. Hartunian, R. A.; and Thompson, W. P.: Nonequilibrium Stagnation Point Heat Transfer Including Surface Catalysis. AIAA Paper No. 63-464, AIAA Conference on Physics of Entry into Planetary Atmospheres, M.I.T., Aug. 1963.

46. Reddy, N. M.: The Use of Self-Calibrating Catalytic Probes to Measure Free-Stream Atom Concentration in a Hypersonic Flow. NASA CR-780, May 1967.
47. Hartunian, R. A.: Local Atom Concentrations in Hypersonic Dissociated Flows at Low Densities. Physics of Fluids, vol. 6, no. 3, March 1963, pp. 343-348.
48. Blackman, V. H.: Vibrational Relaxation in O_2 and N_2 . J. Fluid Mechanics, vol. 1, 1956.
49. Inger, George R.: Nonequilibrium - Dissociated Stagnation Point Boundary Layers With Arbitrary Surface Catalycity. Aerospace Corp. Report No. ATN-63(9206)-3, Jan. 1963.
50. Cheng, H. K.: The Blunt-Body Problem in Hypersonic Flow at Low Reynolds Number. CAL Report No. AF-1285-A-10, June 1963.
51. Treanor, Charles E.: Coupling of Vibration and Dissociation in Gas Dynamic Flows. AIAA Paper No. 65-29, AIAA Second Aerospace Sciences Meeting, New York, Jan. 25-27, 1965.
52. Hall, J. Gordon; and Treanor, Charles E.: Nonequilibrium Effects in Supersonic-Nozzle Flows. CAL Technical Report No. 163, March 1968.
53. Phinney, R.: Criterion for Vibrational Freezing in a Nozzle Expansion. AIAA J., vol. 1, no. 2, Feb. 1963, pp. 496-497.
54. Phinney, Ralph: Nondimensional Solutions of Flows With Vibrational Relaxation. AIAA J., vol. 2, no. 2, Feb. 1964, pp. 240-244.
55. Bray, K. N. C.: Atomic Recombination in a Hypersonic Wind Tunnel Nozzle. J. Fluid Mechanics, vol. 6, July 1959, pp. 1-32.
56. Erickson, Wayne D.: Vibrational-Nonequilibrium Flow of Nitrogen in Hypersonic Nozzles. NASA TN D-1810, June 1963.
57. Ames Research Staff: Equations, Tables, and Charts for Compressible Flow. NACA Report 1135, 1953.
58. Smith, Fred M.; Harrison, Edwin F.; and Lawing, Pierce L.: Description and Initial Calibration of the Langley Hotshot Tunnel With Some Real-Gas Charts for Nitrogen. NASA TN D-2023, Dec. 1963.

APPENDIX

EXPERIMENTAL DATA FOR ALL TESTS

TABLE II.- EXPERIMENTAL RESULTS FROM THE TOTAL CALORIMETER TESTS

Test no.	P _{t,1} (atm)	H _{t,sonic throat} (Btu/lbm)	H _{t,CAL} (Btu/lbm)	T _{t,CAL} (°R)
1	5.82	920	1050	3850
2	6.35	1170	1322	4625
3	7.20	1615	1725	5580
4	7.45	1650	1836	5800
5	3.70	1750	1892	5900
6	7.94	1830	1987	6080
7	8.14	2080	2293	6550
8	8.43	2220	2307	6590
9	9.07	2695	2684	7450
10	9.16	2950	2930	7380
11	9.78	3660	3280	7850
12	7.59	4125	3571	8065
13	11.21	4230	3702	8460
14	5.42	5260	4025	8910

TABLE III.- EXPERIMENTAL RESULTS FROM THE STAGNATION POINT
HEAT-TRANSFER RATE TESTS

Test no.	P _{t,1} (atm)	H _{t,1} (Btu/lbm)	T _{t,1} (°R)	\dot{q} (Btu/ft ² -sec)	P _{t,2} (atm)
15	4.27	840	3130	11.9	6.28×10^{-3}
16	4.67	990	3635	14.6	6.67×10^{-3}
17	5.44	1225	4365	18.1	6.86×10^{-3}
18	5.27	1250	4430	21.9	7.78×10^{-3}
19	5.78	1370	4750	23.1	8.01×10^{-3}
20	5.85	1500	5075	28.9	8.89×10^{-3}
21	6.04	1510	5110	27.0	8.62×10^{-3}
22	6.31	1600	5330	28.7	8.88×10^{-3}
23	6.65	1680	5510	27.1	8.91×10^{-3}
24	6.65	1760	5690	29.9	9.31×10^{-3}
25	6.56	1790	5740	35.0	9.78×10^{-3}
26	6.68	1890	5940	36.9	9.78×10^{-3}
27	9.33	2420	6770	51.6	11.3×10^{-3}
28	9.98	2680	7130	58.4	11.5×10^{-3}
29	10.08	2805	7280	62.4	11.9×10^{-3}
30	7.33	2855	7255	58.0	9.89×10^{-3}
31	10.08	2900	7390	71.3	13.2×10^{-3}
32	9.31	2940	7435	73.6	12.2×10^{-3}
33	4.60	2970	7290	52.0	7.21×10^{-3}

TABLE IV. - EXPERIMENTAL RESULTS FROM THE N₂ VIBRATIONAL
TEMPERATURE TESTS

Test no.	P _{t,1} (atm)	H _{t,1} (Btu/lbm)	T _{t,1} (°R)	T _{V,N₂,∞} (°R)	P _{t,2} (atm)
34	4.35	700	2700	2340	5.11 × 10 ⁻³
35	4.76	905	3350	2430	5.45 × 10 ⁻³
36	5.51	1200	4300	2790	6.32 × 10 ⁻³
37	5.66	1280	4520	2680	6.67 × 10 ⁻³
38	6.02	1410	4860	2810	6.72 × 10 ⁻³
39	6.96	1650	5220	2860	8.07 × 10 ⁻³
40	6.61	1855	5870	3042	7.54 × 10 ⁻³
41	8.46	1970	6065	3170	8.64 × 10 ⁻³
42	7.69	2240	6480	3260	8.53 × 10 ⁻³
43	8.15	2250	6515	3240	8.71 × 10 ⁻³
44	8.25	2520	6910	3530	9.09 × 10 ⁻³
45	8.46	2520	6910	3240	8.92 × 10 ⁻³
46	9.03	2980	7490	3580	9.51 × 10 ⁻³
47	9.51	3130	7685	3530	11.03 × 10 ⁻³

TABLE V.- EXPERIMENTAL RESULTS FROM THE N₂ ROTATIONAL
TEMPERATURE TESTS

Test no.	P _{t,1} (atm)	H _{t,1} (Btu/lbm)	T _{t,1} (°R)	T _{R,N₂,∞} (°R)	P _{t,2} (atm)
48	4.20	700	2665	92.9	5.10×10^{-3}
49	4.86	940	3475	133.2	5.56×10^{-3}
50	5.17	1080	3940	116.7	6.21×10^{-3}
51	6.15	1360	4735	173.0	6.90×10^{-3}
52	6.89	1380	4770	180.9	7.19×10^{-3}
53	6.63	1440	4930	192.2	7.42×10^{-3}
54	8.42	2380	6695	284.1	9.10×10^{-3}
55	8.49	2450	6805	273.9	9.63×10^{-3}
56	8.76	2980	7470	312.2	9.87×10^{-3}
57	9.78	3220	7810	385.6	10.91×10^{-3}
58	9.72	3310	7920	305.8	10.89×10^{-3}

TABLE VI.- EXPERIMENTAL RESULTS FROM THE WALL STATIC
PRESSURE TESTS

Test no.	P _{t,1} (atm)	H _{t,1} (Btu/lbm)	T _{t,1} (°R)	P _∞ (atm)	P _{t,2} (atm)
59	4.13	780	2990	6.11×10^{-5}	7.15×10^{-3}
*60	4.65	1010	3710	7.26×10^{-5}	---
61	5.56	1410	4860	7.95×10^{-5}	9.43×10^{-3}
*62	6.54	1830	5815	9.22×10^{-5}	---
63	6.75	1900	5940	8.80×10^{-5}	11.3×10^{-3}
64	6.99	1920	5975	9.25×10^{-5}	11.4×10^{-3}
65	8.29	2870	7345	10.6×10^{-5}	13.3×10^{-3}
*66	8.92	3070	7595	11.6×10^{-5}	---
67	8.98	3080	7615	11.8×10^{-5}	14.3×10^{-3}
68	9.10	3080	7615	11.3×10^{-5}	13.8×10^{-3}
69	9.32	3115	7670	11.5×10^{-5}	13.8×10^{-3}

*Tunnel empty tests.

TABLE VII.- EXPERIMENTAL RESULTS FROM THE MASS FLOW
PROBE TESTS

Test no.	P _{t,1} (atm)	H _{t,1} (Btu/lbm)	T _{t,1} (°R)	ρ _∞ (slugs/ft ³)	V _∞ (ft/sec)	P _{t,2} (atm)
70	5.54	1290	4555	2.83 × 10 ⁻⁷	7280	6.54 × 10 ⁻³
71	6.22	1610	5345	2.78 × 10 ⁻⁷	7810	7.41 × 10 ⁻³
72	6.51	1725	5580	2.79 × 10 ⁻⁷	7860	7.54 × 10 ⁻³
73	7.27	1730	5580	2.73 × 10 ⁻⁷	8290	8.21 × 10 ⁻³
74	7.35	2080	6175	2.45 × 10 ⁻⁷	9040	8.73 × 10 ⁻³
75	7.40	2080	6175	2.47 × 10 ⁻⁷	8990	8.72 × 10 ⁻³
76	8.04	2460	6805	2.34 × 10 ⁻⁷	9570	9.36 × 10 ⁻³
77	8.45	2520	6875	2.46 × 10 ⁻⁷	9550	9.80 × 10 ⁻³
78	8.08	2560	6930	2.36 × 10 ⁻⁷	9760	9.81 × 10 ⁻³
79	8.26	2720	7165	2.26 × 10 ⁻⁷	9960	9.76 × 10 ⁻³
80	10.05	3290	7900	2.06 × 10 ⁻⁷	11430	11.8 × 10 ⁻³
81	9.28	3310	7940	2.08 × 10 ⁻⁷	11300	11.6 × 10 ⁻³
82	9.38	3510	8225	2.15 × 10 ⁻⁷	11280	12.0 × 10 ⁻³